



THE UNIVERSITY OF QUEENSLAND
A U S T R A L I A

ON-CHIP SUPERFLUID VORTEX GENERATORS

Luke Kelly

Under the supervision of
Dr. Christopher Baker & Prof. Warwick Bowen

A THESIS SUBMITTED TO THE UNIVERSITY OF QUEENSLAND IN PARTIAL FULFILMENT
OF THE DEGREE OF BACHELOR OF ADVANCED SCIENCE WITH HONOURS
SCHOOL OF MATHEMATICS AND PHYSICS
NOVEMBER 2024

© Luke Kelly, 2024.

Typeset in L^AT_EX 2_ε.

The work presented in this Thesis is, to the best of my knowledge and belief original, except as acknowledged in the text, and has not been submitted either in whole or in part, for a degree at this or any other university.

A handwritten signature in black ink, appearing to read "Luke Kelly".

Luke Kelly

Abstract

Single quanta of circulation in bulk superfluid helium-4 were first observed over 60 years ago. Today, 2D superfluids — like thin-film superfluid helium — are rich in interesting physics and are studied extensively. However, at ultra cold temperatures and incredibly small fluid volumes, they are challenging to observe and control experimentally. Because of these difficulties, the quantisation of circulation in 2D superfluid helium is a phenomenon yet to be observed experimentally with single quanta resolution. This thesis presents work completed in moving towards detecting single quanta of circulation in 2D superfluid helium-4. This builds upon existing expertise in precision sensing of thin-film superfluid helium-4 dynamics using cavity optomechanics. Investigation and design of a novel whispering gallery mode micro-resonator device is conducted, numerically and experimentally, covering Gross-Pitaevskii simulations and nano-fabrication processes. Also presented is a novel method in calculating the surface profile of many quantum vortices in these thin-films accounting for surface tension, progressing towards real-time, non-destructive single vortex detection.

List of Publications

Publication in preparation.

D. Harvey, L. Kelly et al. “Vortex-vortex interactions mediated through surface tension”.

Acknowledgements

Its hard for me to overstate my appreciation to my supervisors Dr. Chris Baker and Prof. Warwick Bowen. Both of you have been exceptional supervisors, encouraging me to trust my own ability and guiding me towards excellence in my work. And just as importantly, you've be down-to-earth and fun people to work with. I truly think I couldn't pick a better set of supervisors.

I can't thank everyone in the superfluids group and QOL lab enough for the help you've given me this year. In particular, I am practically indebted to Nicole Luu for the extensive help in the lab, my project would not have happened without your efforts in the clean room.

I'd like to also thank Dr. Matt Reeves for the incredibly useful discussions on the computational aspects of this project, and for being a big inspiration for me moving into superfluid physics. I am very appreciative for you and Prof. Matthew Davis' supervision of my summer project in the BEC group leading into my honours which gave me a very useful background for this thesis.

I can't imagine my project with my close friends that have had to endure my tireless yapping on about how much fun I've had with my work. I also can't imagine how I spent much of my undergrad not know you guys, but I couldn't be more appreciative of having you around.

It almost goes without saying, but I appreciate all the support from my family over the last four years. The feigned interest in topics you've never heard of is always appreciated, though be prepared for those topics to become even more niche.

Contents

Abstract	v
List of Publications	vii
Acknowledgements	ix
List of Figures	xiii
List of Tables	xix
List of Symbols	xxi
1 Introduction	1
2 Superfluid helium	3
2.1 The two-fluid model	3
2.2 Quantum fluids	4
2.3 The fountain pressure effect	5
2.4 Superfluid acoustics	5
2.4.1 First, second, and fourth sound	5
2.5 Third sound and superfluid ^4He thin-films	6
3 Cavity optomechanics	7
3.1 The simple harmonic oscillator	7
3.2 The damped harmonic oscillator	8
3.3 Optical cavities	10
3.4 Quantum optomechanics — input-output theory	10
3.5 Whispering gallery optomechanical sensing	11
3.5.1 Superfluid helium in an optomechanical system	13
3.5.2 Sensing superfluid vortices optomechanically	14
3.6 Whispering gallery mode micro-cavities in superfluid optomechanics	14
4 Angular vortex generators	17
4.1 Basic principles of an AVG	17
4.2 Computational investigation of superfluid helium dynamics in integrated photonic devices	18

4.2.1	Potential flow theory	18
4.2.2	Gross-Pitaevskii simulations	20
5	Device fabrication and experimental implementation	29
5.1	Fabrication process overview	30
5.2	Designing integrated photonic devices	31
5.2.1	Device dimensions and details	31
5.2.2	Implementation of on-chip optical coupling	32
5.3	Characterisation of devices	34
5.3.1	Optical coupling and data acquisition	34
5.3.2	Fabrication issues and design iterating	36
5.3.3	Successful fabrication	38
6	Surface tension and superfluid helium thin-films	43
6.1	Real-time vortex microscopy for superfluid ^4He	43
6.2	Surface tension in superfluid helium thin-films	44
6.3	Vortices in ^4He thin-films with surface tension	46
6.4	Superfluid helium thin-film energies and displaced volumes of vortices	47
6.5	Single vortex traps for superfluid ^4He	48
7	Outlook and Conclusion	51
	References	53

List of Figures

- 4.2 Initial generation of a like-signed (positively signed) vortex cluster at superfluid velocities slightly above the critical velocity v_c . Evolution of longer times sees a (negatively signed) cluster form, originating from the ‘corner’ shallower break angle of the injecting arm incident on the outer ring, as predicted from potential flow modelling (see Fig. 4.1). Continued evolution sees repeated oscillation of these vortex streets, with larger driving strengths leading to smaller cluster sizes i.e. vortex-antivortex pair production. 24
- 4.3 Phase windings diagram of lock circulation in a superfluid. **(a)** A single ‘charge’ of circulation (one period of 2π phase) around a point defect — a quantum vortex. **(b)** A multi-charge circulation around a larger engineered topological defect, similar to the form discussed in the geometry of angular vortex generators. 26
- 4.4 **(a)** Wavefunction density ($|\Psi|^2$) snap shots of ‘free dynamics’ after an initial drive of constant strength from the ground state **(a, i)** until $\bar{t} = 8,000$ **(a, ii)**. Localised areas of vanishing density are topological quantised vortices. A small amount of damping is localised by an approximated penetration depth of guided light at 1550 nm in the projected AVG photonic device sizes. **(b)** Wavefunction phase snap shots across simulation time. Closed loops of integer steps of 2π of the phase around the central defect is a representation of quantised circulation, whilst loops around point defects are vortices. At $\bar{t} = 2,500$, the number of vortices are $n^+ = 34$ and $n^- = 24$ for positively and negatively signed vortices, respectively. At longer time scales vortices continue to mix and annihilate. At $\bar{t} = 10,000$, $n^+ = 17$ and $n^- = 10$, where several κ of locked circulation can be observed around the annulus (see Fig. 4.3). 27
- 4.5 **(a)** Comparison of different initial driving durations, with the wavefunction densities upon evolving the un-driven system under gentle damping at the edge of the annulus. **(b)** The respective systems’ phase profile after 10,000 time steps of evolution. As per Fig. 4.4, **(b,i)** displays the vortex numbers $n^+ = 17$ and $n^- = 10$, though the longer initial drive **(b,ii)** leads to $n^+ = n^- = 19$, with a significantly larger value of locked κ observed around the annulus. It should be noted here that the net locked circulation is resultant of vortices annihilating with their images, which is not necessarily depicted through the presence of a net difference of signed vortex number. 28
- 5.1 **(a)** 1D photonic crystal ‘wave tank’ to study highly non-linear superfluid helium hydrodynamics. The optical cavity (see *) enables precision control and measurement of superfluid helium thin-films, providing a platform to study unique fluid physics at unprecedented wave size aspect ratios. **b** Superfluid helium ‘Tesla valves’ with precision control and measurement enabled by similar optical cavities in **(a)**, where two different resonant frequencies enable driving of ‘forward’ and ‘reverse’ valve directions. These complex geometries are a platform to study turbulence-dependent classical fluid phenomena in the quantum regime of superfluid helium, where quantum turbulence is not well understood by the characteristic lack of viscosity in superfluids. 30
- 5.2 Example CAD drawing of an investigated device design (d3) using KLayout. 33

6.1	Proposed vortex microscopy detection scheme for real-time, non-destructive imaging. (a) General experimental implementation of interferometric scattering microscopy (iSCAT) for superfluid helium vortex detection, enabled by the (weak) interaction of light with vortex ‘dimples’. (b) Rendered diagram of superfluid helium thin-film with microscope objective. Credit: Dr. C. G. Baker.	44
6.2	Iterative numerical approach in solving the surface profile of a vortex in a superfluid helium thin-film with surface tension. Locally adjusting the film height dependent on the chemical potential error (a) ‘anneals’ the surface of the film, and well approximates the exact solution for a single vortex (b) for small enough chemical potential error ($\sim 1\%$), enabling the investigation of surface tension for many vortices [10].	47
6.3	Iteratively solved solutions of vortex-antivortex pairs in a superfluid helium thin-film with the inclusion of surface tension separated by a distance Δx , see Eq. 6.3. (a) A cross-section of the 3D surface reveals a drastic change in the shape of the ‘dimple’ a vortex leaves on the surface when compared to a surface tension-free solution. (b) 3D surface plot of vortex-antivortex pair and the corresponding velocity streamlines of the quantum vortices.	48
6.4	Rendition of gold deposited on a silica substrate demonstrating proposed vortex trapping through the ‘fluid well’ cause by the stronger interaction of superfluid helium with gold than silica. Several gold rings are depicted, where the proposal to apply a voltage across these electrodes is made to electrically tune the height of the trap. Credit: Dr. C. G. Baker.	49
6.5	a Cross-sections of a vortex positions in, on, and far away from a superfluid well induced by locally increased van der Waals interactions of the substrate (see Fig. 6.4). (b) The calculated total energy of the film for increasing radial position of the vortex from the centre of the well, according to Eq. 6.16.	50

List of Tables

- 5.1 Fabricated device design dimensions and features. *Tapered injecting arm design involves ‘subtraction’ of two eccentric disks of same (or different) radii, leading to injecting arm of non-constant width (see Fig. 5.2 and Fig. 5.8). . . 32

List of Symbols

The following list is neither exhaustive nor exclusive, but may be helpful.

Abbreviations

AVG	Angular Vortex Generator
BKT	Berezinskii–Kosterlitz–Thouless
BEC	Bose-Einstein Condensate
EBL	Electron Beam Lithography
EOM	Equation of Motion
FSR	Free Spectral Range
FWHM	Full Width at Half Maximum
HF	Hydrogen-Fluoride
SOI	Silicon on Insulator
WG	Wave Guide
WGM	Whispering Gallery Mode

Symbols

ρ	Density
ρ_n	Normal fluid fraction density
ρ_s	Superfluid fraction density
m	Mass
$m^4\text{He}$	Mass of ${}^4\text{He}$
\vec{p}	Momentum

\vec{v}_s	Superfluid Velocity
κ	Circulation, Total Optical Loss Rate
ΔP_f	Fountain Pressure
S	Entropy
T	Temperature
μ	Chemical Potential
k	Wave Number, Spring Constant
d	Film Thickness
α_{vdW}	van der Waals Coefficient
U	Potential Energy
ω_0	Resonant Frequency
ω_{cav}	Cavity Frequency
$\Delta\omega_{\text{FSR}}$	Frequency Free Spectral Range
λ	Wavelength
λ_0	Resonant Wavelength
$\Delta\lambda_{\text{FSR}}$	Wavelength Free Spectral Range
Γ	Damping Rate
Q	Quality Factor
\mathcal{F}	Optical Finesse
τ	Lifetime Characteristic Time Scale
\hat{a}	Annihilation Operator
\hat{a}^\dagger	Creation Operator
Δ	Detuning
i	Imaginary Unit
\mathcal{R}	Reflection Amplitude
ε	Dielectric Constant
\vec{E}	Electric Field

n	Refractive Index
n_g	Group Refractive Index
n_{eff}	Effective Refractive Index
\hbar	Planck's Constant
c	Speed of Light

1

Introduction

Superfluid helium has been an area of interest since the observation of the non-classical behaviour of liquid helium below 2.2 K in 1938 [11]. The proposal by F. London that the ‘superfluid’, as coined by Kapitza [12], was the first observation of a Bose-Einstein condensate (BEC) sparked massive interest in understanding the underlying physics [13]. Superfluids, a BEC of interacting particles, are described by a macroscopic wavefunction and are inherently quantum fluids. There is no current microscopic theory describing superfluids, though their hydrodynamics are well approximated by the ‘two-fluid model’, introduced by L. Tisza in 1938 and further revised by L. Landau in 1941 [14, 15].

Many properties of superfluid hydrodynamics are non-classical and non-linear, making the area rich in newly discovered physics over the last century. The defining lack of viscosity has pushed extensive theoretical and experimental investigation into how turbulence arises in superfluids [8, 16–21]. Moreover, the quantum mechanical nature of superfluids allows for quantised vortices to emerge, with quantised circulation around topological defects. The dynamics and existence of vortices in superfluids have been shown to be fundamental in understanding them, especially in the microscopic regime [8, 18]. It was many decades after their initial discovery that 2-dimensional (2D) superfluid ‘films’ had been shown to theoretically exist by the Berezinskii–Kosterlitz–Thouless mechanism. This work contributed to the 2016 Nobel prize in physics, reigniting interest in superfluids in the last decade [22–25]. These hydrodynamic and quantum properties have been observed in the bulk phase of superfluid helium, though experimentally probing microscopic behaviour has proved to be challenging, with so-called ‘quasi-2D’ film regimes only being accessible in recent years [8, 19].

In the last 30 years, improved fabrication techniques have allowed the development of optically and mechanically high quality ‘micro-cavities’, which, coupled with the exploitation of radiation pressure forces, allows for the precise measurement of optomechanical systems and application of techniques, such as laser cooling and amplification [26–29]. Since the

emergence of micro- and nano-fabrication, whispering gallery mode (WGM) resonators have proved to be a desirable platform to study the effects of radiation pressure forces in many optomechanical systems [28, 30]. Whispering gallery mode resonators confine an optical field to the edge of a radially symmetric dielectric medium, and are named after their likeness to ‘whispering galleries’, where acoustic waves are guided by curved walls of a building. The guided optical field in the resonator has a number of ‘allowed’ optical modes dependent on the path length (circumference) of the guided light and refractive index of the medium. As such, mechanically changing the size of the resonator or changing its (effective) refractive index can lead to frequency shifts in the allowed modes. Depending on the geometry of the resonator, these frequency shifts can be used to detect precise changes in the optomechanical system [4, 31].

This branch of optomechanics brings the advantage of precision to many areas of sensing, including; magnetometers, bio-sensing, single molecule detection, and thermometers [26, 32, 33]. These incredibly precise sensors rely on tiny ‘forces’ applied to the WGM resonator, which arise from minute perturbations in the optomechanical system from the presence of an external medium or field. Moreover, recent studies in applying the precision sensing schemes of optomechanics to superfluids (superfluid optomechanics) have shown it to be a useful platform in probing the microscopic behaviour of superfluid helium [34–37]. In this area, superfluid helium is used as an optomechanical material, where the dynamical behaviour of the superfluid acts as a mechanical degree of freedom, allowing for the investigation of superfluid helium in volumetric regimes that were previously unreachable. This review will cover applying the principles of WGM optomechanics to superfluids as a platform to study thin-film superfluid helium.

This thesis presents general relevant background of superfluids — namely superfluid helium-4 — in context of the field of superfluid optomechanics. The development, design, and optimisation of a novel integrated photonic device is laid out. These devices are engineered for controllable vortex generation to produce net quantised circulation in 2D superfluid helium thin-films. Given the name ‘angular vortex generators’, the computational simulation of relevant superfluid dynamics using the damped Gross-Pitaevskii equation for a modelled experimental environment is discussed. Moreover, the results of these simulations are used to design these device geometries into ‘on-chip’ integrated photonic circuits. Preliminary fabrication and device characterisation is conducted, focusing on optimisation of relevant optical characteristics in the pursuit of implementation into experiment using superfluid optomechanics. Finally, numerical work on the effects of surface tension on vortices’ surface profile in superfluid helium thin-films is presented, progressing towards real-time, non-destructive single vortex detection.

2

Superfluid helium

The following section is an outline of relevant theoretical background on superfluids and optomechanics required to understand some of the experimental investigation of WGM resonators for thin-film superfluid optomechanics later discussed in this work. A basic introduction to superfluid helium discussed, covering acoustic and optical properties. These topics are an essential background in experimental superfluid optomechanics for thin-film helium, which will be used in this work to investigate 2D superfluid helium.

2.1 The two-fluid model

Early work around superfluids and superconductivity led to the introduction of the two-fluid model to describe many properties of these systems. Initially introduced by Tisza in 1938 and further refined by Landau in 1941, the model is used extensively and very successfully to describe and model the hydrodynamics of superfluids in place of a microscopic theory [14, 15]. Here a finite temperature superfluid is described by a combination of an idealised normal-fluid phase and a perfect superfluid phase, with the total fluid density being described by

$$\rho = \rho_n + \rho_s, \tag{2.1}$$

where ρ_n and ρ_s are the densities of the normal and superfluid fraction, respectively. This model presents the superfluid phase as particles obeying a single quantum state of a Bose liquid, and the normal-fluid phase describes the elementary excitations of the liquid. At the ‘lambda’ point ($T = T_\lambda$), the superfluid fraction density goes to zero and, similarly, in the zero temperature limit the normal-fluid fraction density goes to zero. The viscosity of the fluid is attributed to the elementary excitations of the normal-fluid fraction, and so in the zero temperature limit, the viscosity vanishes along with ρ_n . For similar reasons, the entropy of the fluid also vanishes with ρ_n [15]. The normal-fluid fraction’s excitations

transfer momentum to its container, producing a ‘viscous friction’, an effective viscosity in the finite temperature regime for a bulk phase of superfluid.

2.2 Quantum fluids

Liquid ${}^4\text{He}$ is a collection of strongly correlated bosons, which behaves as a classical liquid until its transition temperature $T_\lambda = 2.17$ K, where it begins to exhibit superfluidity [13]. Below this temperature, particles in the liquid occupy the same quantum state and the system begins to display peculiar properties in comparison to ordinary fluids. Famously, the fluid’s viscosity vanishes, allowing for flow through tiny capillaries due to the dominating van der Waals interaction with the walls of the capillary [11]. Superfluids are rich in unique phenomena not seen in classical fluids, but arguably the most interesting is the superfluid fountain pressure effect, where superfluids have a reversed direction of flow due to applied heat compared to classical fluids [11, 13]. Superfluids are described by a macroscopic wavefunction Ψ , with a complex phase parameter such that

$$\Psi(\vec{r}) = \Psi_0 e^{i\Phi(\vec{r})}, \quad (2.2)$$

with $\Phi(\vec{r})$ describing the phase and being real valued, and Ψ_0 being a (typically) constant amplitude [13]. Contributions of the perfect superfluid and perfect normal component to the two-fluid model density (Eq. 2.1) are attributed to the complex phase parameter of Ψ . The normalisation of the wavefunction is often done using the proportion of the perfect superfluid density [13]. For example, the normalisation for a wavefunction pertaining to superfluid helium-4 can be taken as

$$|\Psi|^2 = \frac{\rho_s}{m_{\text{He}}^4}. \quad (2.3)$$

Acting the momentum operator on the wavefunction (in the Schrödinger picture) returns

$$\hat{p}\Psi = -i\hbar\nabla\Psi = \hbar\nabla\Phi\Psi, \quad (2.4)$$

from Eq. 2.2, where \hbar is the reduced Planck’s constant. From the momentum, the superfluid velocity \vec{v}_s can be obtained

$$\vec{v}_s = \frac{\hbar}{m_{\text{He}}^4} \nabla\Phi. \quad (2.5)$$

Around ‘simply-connected’ domains, superfluids are irrotational, meaning the circulation is zero, with the circulation being

$$\kappa = \oint \vec{v}_s d\vec{r} = \oint \frac{\hbar}{m} \nabla\Phi d\vec{r}, \quad (2.6)$$

which is the curl of the superfluid velocity. This is zero as it is simply the curl of the gradient of the phase ($\text{curl } \vec{v}_s \propto \text{curl } \nabla\Phi = 0$). Around ‘multiply-connected’ domains, Eq. 2.6 reduces to

$$\kappa = \frac{\hbar}{m} \nabla\Phi, \quad (2.7)$$

where $\nabla\Phi$ must be single valued at each point in the fluid, which gives $\nabla\Phi = 2\pi n$, where n is an integer. This again reduces the circulation of a superfluid around a multiply connected domain to

$$\kappa = n \frac{h}{m}, \quad (2.8)$$

where h is Planck's constant. From Eq. 2.8, it is evident that the circulation of a superfluid around a multiply connected domain is quantised in units of h/m and the wavefunction is no longer irrotational. These multiply-connected domains appear in practice as topological defects, such as localised displaced fluid density (leading to a quantum vortex) or physical obstacles in the fluid. The detection of single quanta of circulation in superfluid helium was famously first demonstrated by W. F. Vinen through the lifting of degeneracy in counter-rotating sound modes around a thin vibrating wire in a rotated superfluid [38].

2.3 The fountain pressure effect

Contrary to the behaviour of classical fluids, superfluids flow *against* temperature gradients due to the ‘fountain pressure’ effect, with pressure ΔP_f . This is a thermo-mechanical effect stemming from the superfluid fraction of the fluid carrying no entropy, and was first observed in 1938 when superfluid ^4He flowed towards a heat source [11]. This behaviour is opposite to what one might expect from a classical fluid, and is described by the relation

$$\Delta P_f = \rho_s S \Delta T, \quad (2.9)$$

where $S = S_n$ is the entropy of the total liquid (hence the entropy of the normal-fluid fraction) and ΔT is a temperature differential. By extension of Eq. 2.9, applying a pressure gradient also induces a temperature gradient in the fluid, this phenomenon being named the ‘mechano-caloric’ effect. This behaviour is critical in understanding the dynamics of a superfluid and has been exploited in recent experiments to precisely control the motion of superfluid ^4He in micro-cavity optomechanical systems [7, 8, 39–41].

2.4 Superfluid acoustics

The two-fluid model for superfluids permits several distinct regimes in which different forms of sound can propagate. Each regime is defined by whether specific sound modes are allowed in the system, which for certain geometries can allow for access to more than one regime at a time. The distinction between these regimes is a useful tool in describing the hydrodynamics of superfluids. The following section will briefly discuss them, with focus placed on third sound, as well as a brief discussion on superfluid surface tension in the third sound regime. See [13] for further detail on superfluid sound regimes.

2.4.1 First, second, and fourth sound

First sound waves are longitudinal compression waves, analogous to ‘ordinary’ sound waves in a fluid. This regime is seen in bulk superfluids, more specifically, when the sound wave

period ($1/\omega$) is long compared to the collision time τ of the (quasi-) particles in the fluid. Here the compression wave affects both the normal and superfluid fractions equally. The speed of first sound v_1 varies with temperature; at the $T = T_\lambda$ it is 220 m/s, and in the zero temperature limit, $v_1 = 238$ m/s.

Out-of-phase oscillation of the superfluid fraction and normal fluid fraction densities give rise to **second** sound, which is characteristic of superfluids (more specifically the two-fluid model). These oscillations occur in such a way to keep the total pressure, and by extension the total density, constant. The speed of second sound varies much more than first sound, but v_2 can range from 10 m/s at T_λ , up to 150 m/s in the zero temperature limit. Fluctuations in the superfluid density implies that second sound waves are equivalently temperature fluctuations, since the superfluid fraction carries no entropy (see Eq. 2.9).

When considering flow in narrow, confined geometries, the normal fluid fraction ρ_n becomes ‘viscously’ clamped, with the superfluid fraction ρ_s making up the entirety of the fluid. This is the regime of **fourth** sound, and the confining geometry allows for only density fluctuations of the superfluid fraction, rather than height fluctuations, contrary to the similarly viscously clamped regime of **third** sound investigated in the following section. Similarly to second sound, these density fluctuations are equivalently temperature fluctuations. Moreover, in the zero temperature limit with vanishing normal fluid fraction, first and fourth sound become identical regimes.

2.5 Third sound and superfluid ^4He thin-films

With analogous behaviour to the hydrodynamics of shallow water waves, third sound is a regime most often attributed to surface waves on a superfluid thin-film. With the normal fluid fraction viscously clamped, the fluid participating in motion is almost entirely superfluid. The speed of third sound in the zero temperature limit is given by

$$v_3 = \sqrt{\frac{\rho_s}{\rho} \frac{3\alpha_{\text{vdW}}}{d^3}}, \quad (2.10)$$

where α_{vdW} is the van der Waals coefficient and d is the film thickness. For sufficiently thin superfluid films ($d \sim 10^{-8}$), the van der Waals interaction between the fluid and the substrate dominates the interaction between gravity and the fluid, with the van der Waals interaction with the film (when only considering sound)

$$\mu_{\text{vdW}} = \frac{\alpha_{\text{vdW}}}{(d + \eta)^3} - \frac{\alpha_{\text{vdW}}}{d^3}, \quad (2.11)$$

where η is the height of the surface wave from the average film thickness d . For small amplitude sound waves, $\eta \ll d$, this can be approximated by Taylor expanding, keeping only the first term

$$\mu_{\text{vdW}} \approx -\frac{3\alpha_{\text{vdW}}}{d^4}\eta. \quad (2.12)$$

This shallow wave result can be viewed as a shallow water wave with an effective restoring force, where for water waves $\mu_g = g\eta$. This small amplitude approximation is both useful and reasonable for current low amplitude third sound superfluid experiments [7, 42].

3

Cavity optomechanics

Cavity optomechanics makes use of the coupled interaction of light and a mechanical degree of freedom as a basis for interferometry. This idea is most famously employed in many gravitational wave detection observatories, like LIGO or VIRGO [31, 35]. Minute interactions with light and matter are detectable in these systems, namely through the effect of radiation pressure on mechanical oscillators. ‘On-chip’ platforms have been designed in the last few decades that enable precision optomechanical sensing and widespread investigation in this field. Recent efforts have been made to extend these sensing applications to other fields, particularly to biological sensing. Applying these principles to superfluids provides a platform to much more precisely detect their dynamics than current popular schemes such as capacitive control and sensing [43, 44]. The following section will build a framework to probe the microscopic phenomena of superfluids and to understand the mechanisms behind precision control and measurement of superfluids, demonstrated in recent studies [8, 35, 39, 42].

3.1 The simple harmonic oscillator

To build up towards understanding the effects of superfluid on an optomechanical system, it is useful to start by understanding basic optomechanical systems. Let us consider a slightly modified Fabry-Pérot cavity (a very basic optical cavity, consisting of two opposing mirrors) where one mirror is allowed to move slightly. This is visualised in Fig. 3.1, with the movable mirror modelled simply as a mass on a spring. A mass on a spring is well understood throughout physics; with a linear restoring force, it represents many physical systems near their energy minima (for small perturbations). Describing the mass as a simple harmonic oscillator, the potential energy of the system can be written as

$$U(x) = \frac{1}{2}kx^2, \quad (3.1)$$

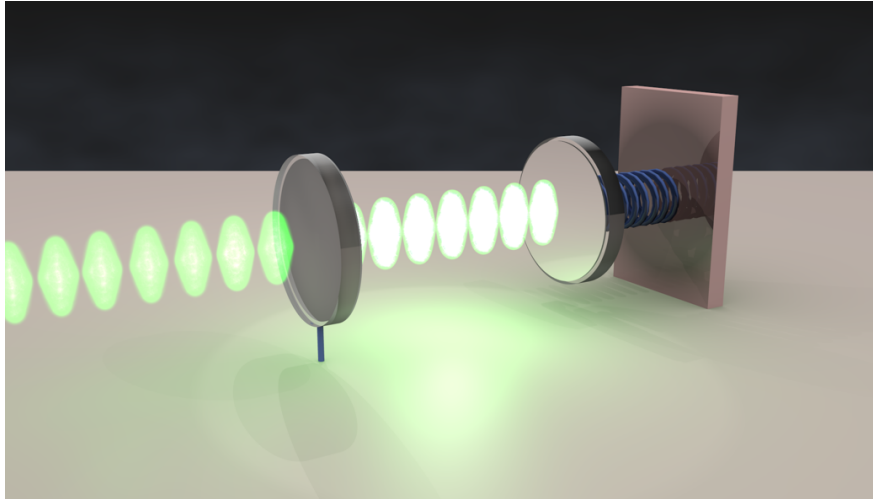


Fig. 3.1: Fabry-Pérot Cavity model illustration. Mechanical component of the cavity is represented as a movable mirror (mass) on a spring, with light entering and exiting from the fixed mirror. Light that enters the cavity is resonantly enhanced, with the resonance condition being governed by the length of the cavity - a dynamic parameter by the means of radiation pressure and a mechanical degree of freedom. Credit: Dr. C. G. Baker.

with spring constant k describing the strength of the restoring force. To obtain the equation of motion (EOM) for this system, Newton's second law can be used in conjunction with deriving a conservative force from the potential energy, which is done very simply

$$F(x) = -\frac{dU(x)}{dx} = -kx \quad (3.2)$$

$$\implies m\ddot{x} + kx = 0. \quad (3.3)$$

For a positive spring constant k , this second-order ordinary differential equation (ODE) produces the family of solutions

$$x(t) = C_1 \sin(\omega_0 t) + C_2 \cos(\omega_0 t), \quad (3.4)$$

where $\omega_0 = \sqrt{k/m}$ is the ‘resonant’ frequency, and constants C_1 and C_2 are determined by the initial conditions. This results in an indefinitely oscillating system, which is not physically realisable in a system with loss mechanisms. Energetic losses are inevitable in mechanical and optical systems, with loss pathways mostly being encapsulated by photon losses through scattering and absorption optically, and by friction or drag mechanically.

3.2 The damped harmonic oscillator

To further improve the applicability of the simple harmonic oscillator to the Fabry-Pérot cavity, a damping term can be added to the EOM. This system is known as a ‘damped harmonic oscillator’ (DHO), where we account for friction with a damping coefficient Γ , and it can be implemented into Eq. 3.3

$$m\ddot{x} - m\Gamma\dot{x} + kx = 0. \quad (3.5)$$

ODE's of this form can be solved using an exponential ansatz solution $x = Ce^{\xi t}$, similarly to the SHO. Substituting this ansatz into the EOM returns

$$\begin{aligned} m\xi^2 e^{\xi t} - m\Gamma\xi e^{\xi t} + ke^{\xi t} &= 0 \\ \implies \xi^2 - \Gamma\xi + \omega_0^2 &= 0. \end{aligned} \quad (3.6)$$

Here, the roots of the characteristic polynomial are given by the quadratic formula as

$$\xi = \frac{-\Gamma \pm \sqrt{\Gamma^2 - 4\omega_0^2}}{2}. \quad (3.7)$$

An under-, over-, or critically-damped system is characterised by the subsequent sign (or value) inside the radical term, respectively being negative, positive and zero. An under-damped system has the solution

$$x(t) = C_1 e^{-\Gamma t/2} \sin(\omega t + \phi), \quad (3.8)$$

with the natural frequency $\omega = \frac{1}{2}\sqrt{4\omega_0^2 - \Gamma^2}$. The proportion of energy lost per oscillation for the DHO is characterised by the (mechanical) Q-factor, which is simply the ratio of the stored energy of the resonator and the energy lost per cycle

$$Q = 2\pi \frac{E_{\text{resonator}}}{E_{\text{lost/cycle}}}. \quad (3.9)$$

Particularly ‘high’ Q factors can be approximated in frequency space by comparing the Full Width at Half Maximum (FWHM) to the natural frequency of the oscillator $Q \approx \frac{\omega}{\Delta\omega}$. Q-factors are dimensionless and they provide a quantitative description of how ‘efficiently’ a device resonates. However, optomechanical resonators have an associated ‘driving’ force acting on the mechanical resonator - the optical field through radiation pressure forces. Consider actively driving a DHO

$$m\ddot{x} - m\Gamma\dot{x} + kx = F_{\text{drive}}. \quad (3.10)$$

Looking specifically at a sinusoidal drive, setting $F = \omega_0^2 C_1 \sin(\omega_d t)$, where ω_d is the driving frequency. Now to solve the inhomogeneous ODE of Eq. 3.10, a solution of the form $x(t) = x(t)_H + x(t)_I$ can be assumed. The inhomogeneous part of the solution can be found by assuming it takes the form of the driving force

$$x(t)_I = C_2 \sin(\omega_d t + \phi_d), \quad (3.11)$$

and $x(t)_H$ has already been found. From these solutions the frequency response of the driven oscillator, $R(\omega) = C_2/C_1$, can be found by substituting the solution into Eq. 3.10

$$R(\omega) = \frac{\omega_0^2}{\sqrt{(\omega_0^2 - \omega_d^2)^2 + \Gamma^2 \omega_d^2}}. \quad (3.12)$$

This frequency response is a useful parameter in understanding the damped harmonic oscillator and turns out to have the same EOM as the mechanical resonator looked at so far. We will find that the frequency response is also useful in understanding the Fabry-Pérot cavity that we are trying to model.

3.3 Optical cavities

Many of the useful properties of an optical cavity are described by the resonance condition of the cavity and the internal photon intensity decay rate [31]. A Fabry-Pérot resonator, for example (see Fig. 3.1), has a series of resonant angular frequencies depending on the path length of the light L , with the resonance condition for a perfect resonator being $\omega_n = n\pi c/L$, where c is the speed of light in the cavity, and n is the integer mode number. This condition allows us to define the ‘Free Spectral Range’ (FSR) of a cavity, describing the spacing between any two resonant frequencies

$$\Delta\omega_{\text{FSR}} = \omega_{n+1} - \omega_n = \pi \frac{c}{L}. \quad (3.13)$$

Internal absorption and scattering mechanisms of the cavity mirrors presents an inherent imperfection of the resonator, where these losses are characterised by an internal photon intensity decay rate, κ . The optical finesse \mathcal{F} of a cavity makes use of κ , the average rate of photon loss, to describe the average number of path lengths taken per photon before decaying out of the cavity,

$$\mathcal{F} = \frac{\Delta\omega_{\text{FSR}}}{\kappa}. \quad (3.14)$$

The optical finesse is a measure of how much energy is lost per round trip of the optical cavity, and is related to the previously discussed Q-factor for the DHO [31], but is now an optical property. Alternatively, the optical Q-factor of a cavity can be defined. This is the average number of oscillations of a photon before it decays out of the cavity (for a single optical mode), ω_{cav} , and makes use of the photon lifetime $\tau = \kappa^{-1}$

$$Q_{\text{opt}} = \omega_{\text{cav}}\tau. \quad (3.15)$$

The decay rate of a cavity is often determined by more than one pathway, where for high-Q cavities, it is useful to describe the total decay rate as a sum of two pathways; $\kappa = \kappa_{\text{ex}} + \kappa_0$, with κ_{ex} describing the *extrinsic* decay rate associated with the coupling of photons into and out of the cavity, and κ_0 the *intrinsic* decay rate — describing all other decay rates associated with internal imperfections of the cavity. Here the extrinsic decay rate describes useful photons that are transmitting information between the cavity and an optical readout, whilst the intrinsic decay rate describes photons that carry information that is lost to the environment.

3.4 Quantum optomechanics — input-output theory

In the case where the dynamics (or time evolution) within the cavity are of interest, it is useful to have a framework for which the dynamics are observable. Input-output theory is a quantum mechanical formulation of optomechanics in the Heisenberg picture, which describes the time evolution of a cavity’s field amplitude \hat{a} , the coupling of light in and out

of the system. The quantum Langevin equation of motion for the field amplitude inside a cavity is [31]

$$\frac{d\hat{a}}{dt} = -\frac{\kappa}{2}\hat{a} + i\Delta\hat{a} + \sqrt{\kappa_{\text{ex}}}\hat{a}_{\text{in}} + \sqrt{\kappa_0}\hat{b}_{\text{in}}, \quad (3.16)$$

where $\Delta = \omega_{\text{laser}} - \omega_{\text{cav}}$ is the detuning of the optical frequency from the resonant frequency of the cavity. The field operator \hat{a}_{in} is a stochastic quantum field describing the a coherent laser drive and the coupling of the vacuum electric field fluctuations into the cavity with decay rate κ_{ex} . The input field \hat{b}_{in} describes the coupling, similar to \hat{a}_{in} , of the cavity to the environment with decay rate κ_0 . The field amplitudes are time dependent and normalised to describe the input power of photons into (and out of) the cavity as

$$P = \hbar\omega_{\text{laser}}\langle\hat{a}_{\text{in}}^\dagger\hat{a}_{\text{in}}\rangle, \quad (3.17)$$

with a similar relation for \hat{b}_{in} . Input-output theory predicts that the output field of a Fabry-Pérot resonator is of the form [31]

$$\hat{a}_{\text{out}} = \hat{a}_{\text{in}} - \sqrt{\kappa_{\text{ex}}}\hat{a}. \quad (3.18)$$

Using Eq. 3.16, one can arrive at an expression for a steady state solution (where $\langle\hat{b}_{\text{in}}\rangle = 0$) for the amplitude field

$$\langle\hat{a}\rangle = \frac{2\sqrt{\kappa_{\text{ex}}}\langle\hat{a}_{\text{in}}\rangle}{\kappa - 2i\Delta}, \quad (3.19)$$

which then with $\langle n \rangle_{\text{cav}} = \langle\hat{a}^\dagger\hat{a}\rangle$ gives the time averaged photon number in the cavity

$$\langle n \rangle_{\text{cav}} = \frac{P}{\hbar\omega_{\text{laser}}} \frac{\kappa_{\text{ex}}}{\Delta^2 + (\kappa/2)^2}. \quad (3.20)$$

Combining Eq. 3.19 with Eq. 3.18 produces the reflection amplitude for a Fabry-Pérot cavity is of the form [31]

$$\mathcal{R} = \frac{\langle\hat{a}_{\text{out}}\rangle}{\langle\hat{a}_{\text{in}}\rangle} = \frac{(\kappa_0 - \kappa_{\text{ex}}) - 2i\Delta}{(\kappa_0 + \kappa_{\text{ex}}) - 2i\Delta}. \quad (3.21)$$

The probability of reflection is then $|\mathcal{R}|^2$, for the case of a Fabry-Pérot cavity. This is the primary measurement of concern for photonic circuits under the input and output intensity of a driving laser. For a critically coupled system (i.e. $\kappa_0 = \kappa$) with no detuning, the measured reflection probability of the cavity is zero. This means if the decay rates are known, then for a fixed input frequency, changes in the resonant frequency can be determined by the optical read out $|\mathcal{R}|^2$ of the cavity.

3.5 Whispering gallery optomechanical sensing

Whispering gallery mode (WGM) resonators are a type of optical cavity that confines light to the circumference of a circular path through total internal reflection — analogous to the

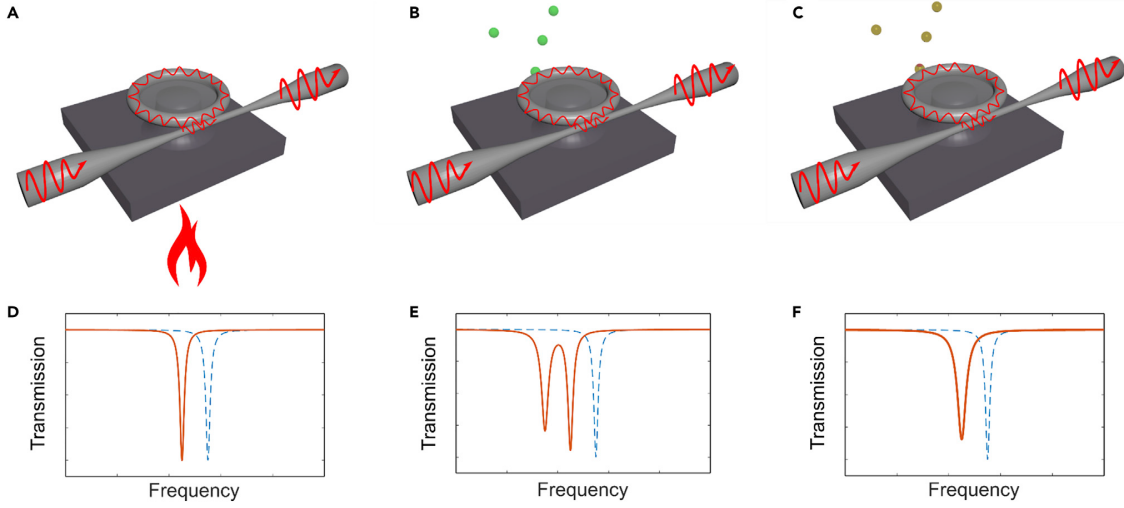


Fig. 3.2: Illustrations of commonly used sensing modalities for a WGM micro-devices (micro-toroid): Mode shift (**A** and **D**) [1], mode splitting (**B** and **E**) [2], and mode broadening (**C** and **F**) [3]. Precise measurement of the position nature of these resonance frequencies can be used to infer changes to the environment of the resonator over time. Figure taken from [4].

Fabry-Pérot cavity. These systems famously get their name from the St. Paul's Cathedral in London, where the curved surrounding walls of the gallery guide even the quite sound of a whisper to the opposite side of the gallery [45]. The optical resonance condition of these cavities relies on constructive interference per round trip of the circumference. Within integrated photonic systems, WGM resonators see a large proportion of the guided light as an evanescent field, travelling in a medium of a different refractive index. In short this leads to the resonance condition

$$2\pi n_g = m\lambda_0, \quad (3.22)$$

where n_g is the group refractive index of the light, m is the azimuthal mode number, and λ_0 the resonance frequency. This group index is often approximated as an ‘effective refractive index’, which highly depends on the specifics of a system. WGM resonators have a vast range of applications to areas in precision sensing; including detecting viruses, proteins, magnetic fields, and nano-mechanical oscillators [4]. These detection schemes typically rely on one of three mechanisms; dispersive coupling, dissipative coupling, or mode splitting. Dispersive coupling involves a change in the effective refractive index of the resonator, which leads to a detectable shift in its resonant frequency. Mode splitting is a frequency ‘splitting’ of the optical modes of the cavity, which can occur through scattered light (by a particle) from one of the (usually degenerate) ‘clockwise’ (CW) or ‘counter-clockwise’ (CCW) optical modes, being scattered into the respective opposite mode direction. Finally, dissipative coupling is simply an increased cavity loss rate due to absorption or scattering of the evanescent field (i.e. a particle), which would manifest as a mode ‘broadening’ around the resonant frequency. These detection schemes, and example optical read-outs, are shown in Fig. 3.2. These sensing schemes offer a well-defined framework to detect the minute perturbations of an optomechanical system caused by the interaction of nano-sized particles with the

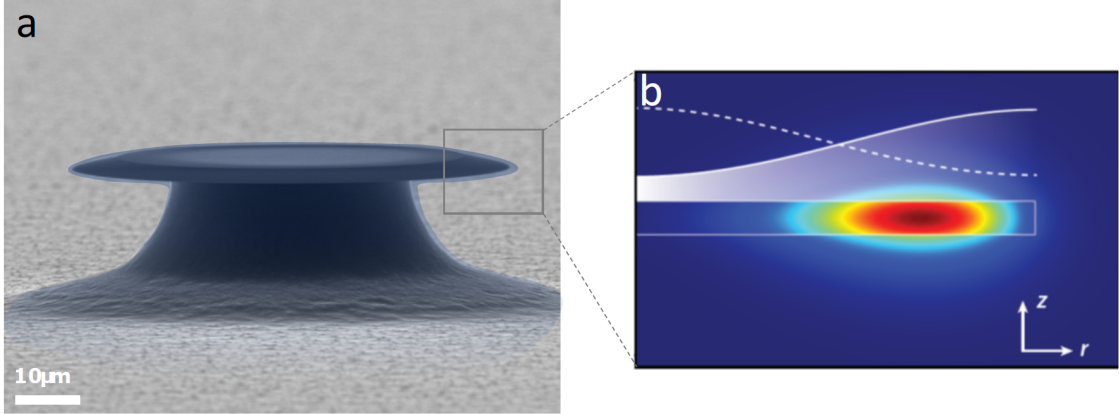


Fig. 3.3: (a) SEM image of a whispering gallery mode micro-disk resonator, illustratively coated with a superfluid thin-film. This, and similar devices, have been used to study thin-film superfluid helium. (b) Cross-section of confined optical field within the outer edge of the disk-resonator. Figure taken from [5].

evanescent field of a WGM resonator. Applying this framework to superfluids allows for the probing of superfluid thin-films with previously unseen precision in superfluid hydrodynamic measurements.

3.5.1 Superfluid helium in an optomechanical system

To implement optomechanical sensing with superfluid ${}^4\text{He}$, the detection schemes previously mentioned (Section 3.5) need to be applied to a superfluid system, and this review will focus on thin-film third sound superfluid-coated WGM resonators. This can be pictured as a thin-film of superfluid coating the surface of a WGM resonator, such as a micro-toroid, or a micro-disk as seen in Fig. 3.3.

Changes in volume of a superfluid thin-film coated resonator may occur in the presence of hydrodynamics like waves or vortices. These volume changes impact the effective refractive index of the optical mode, which is a form of dispersive coupling to the evanescent field. The frequency shift $\Delta\omega$ of a WGM resonance frequency due to the presence of a superfluid thin-film can be approximated to first order by taking the ratio of energy in the perturbing element (i.e. the superfluid film) to the total energy (integrated all space) [35]

$$[t!]\frac{\Delta\omega_{\text{cav}}}{\omega_0} = -\frac{1}{2}\frac{\int_{\text{film Volume}}(\varepsilon_{s.f}-1)|\vec{E}(\vec{r})|^2 d^3\vec{r}}{\int_{\text{all space}}\varepsilon(\vec{r})|\vec{E}(\vec{r})|^2 d^3\vec{r}}. \quad (3.23)$$

Here ω_0 is the unperturbed WGM resonant frequency, $\varepsilon_{s.f} = 1.058$ is the relative permittivity of superfluid helium [46], and $\varepsilon(\vec{r})$ is the relative permittivity. So then, Eq. 3.23 relates the (observable) resonant frequency shift of the cavity to the volume of the superfluid film (numerator integral), providing a mechanism to detect volume changes of the superfluid film.

3.5.2 Sensing superfluid vortices optomechanically

Optical Detection

Free surfaces of superfluids in the presence of a vortex line have been well understood to differ from a ‘flat’ surface as a ‘dimple-like’ depression (see Section 2.4). This occurs in thick- and thin-film superfluids ($d \sim 10^{-9} - 10^{-5}$ m), and has been shown for superfluid ^4He films that were externally rotated to induce quantised circulation, i.e. a vortex [10, 16, 47–49]. Simply put, these dimples displace fluid in the film, changing the total volume and effective refractive index, which in turn affects the frequency response of a resonator (see Eq. 3.23). As such, superfluid vortices have the potential to be detected optically in real-time and non-destructively through dispersive coupling. However, the effect of many vortices on the total film volume is not well-understood (see Section 2.4) and superfluid vortices have yet to be detected this way.

Acoustic Detection

Mode splitting of an acoustic resonator due to vortices in a superfluid thin-film must occur from some breaking of mechanical mode degeneracy in the CW and CCW directions. The presence of a net circulation in the superfluid film is in fact a ‘splitting’ of the CW and CCW superfluid velocity components, and hence, breaking of the mechanical mode degeneracy. Circulation is then a detectable phenomenon for superfluid optomechanics, since any net circulation due to superflow or vortices will result in a frequency splitting of the acoustic mode. Moreover, the quantised nature of superfluid circulation allows for the measurement of the total number of vortices present in the film, which has been experimentally demonstrated for tens of vortices [8].

3.6 Whispering gallery mode micro-cavities in superfluid optomechanics

Whispering gallery mode (WGM) micro-cavities have proven to be a robust platform in study many superfluid helium phenomena in recent works [6–9, 39]. These platforms interface extremely well at the junction of cavity optomechanics and thin-film superfluid helium work. Several variations of WGM resonators are applicable — and even unique — to this field, some of which can be found in Fig. 3.4. Each platform has respective advantages and disadvantages depending on the intended investigation of superfluid helium. The following is a very brief overview of the several WGM micro-cavity platforms seen in Fig. 3.4 — further discussion of ‘micro-annulus’ type resonators can be found in Chapters 4 and 5.

Micro-disks are one of the simplest geometries to design a WGM resonator from. Often fabricated from high refractive index materials like silicon ($n_{\text{Si}} = 3.47$ at 1550 nm and $T = 300$ K), for strongly confined optical fields [50]. These devices are the basis for many optomechanical sensors, not only in superfluid optomechanics [4, 32]. Micro-disks can be as plain as basic disk, and micro- and nano-fabrication techniques are used to support the device

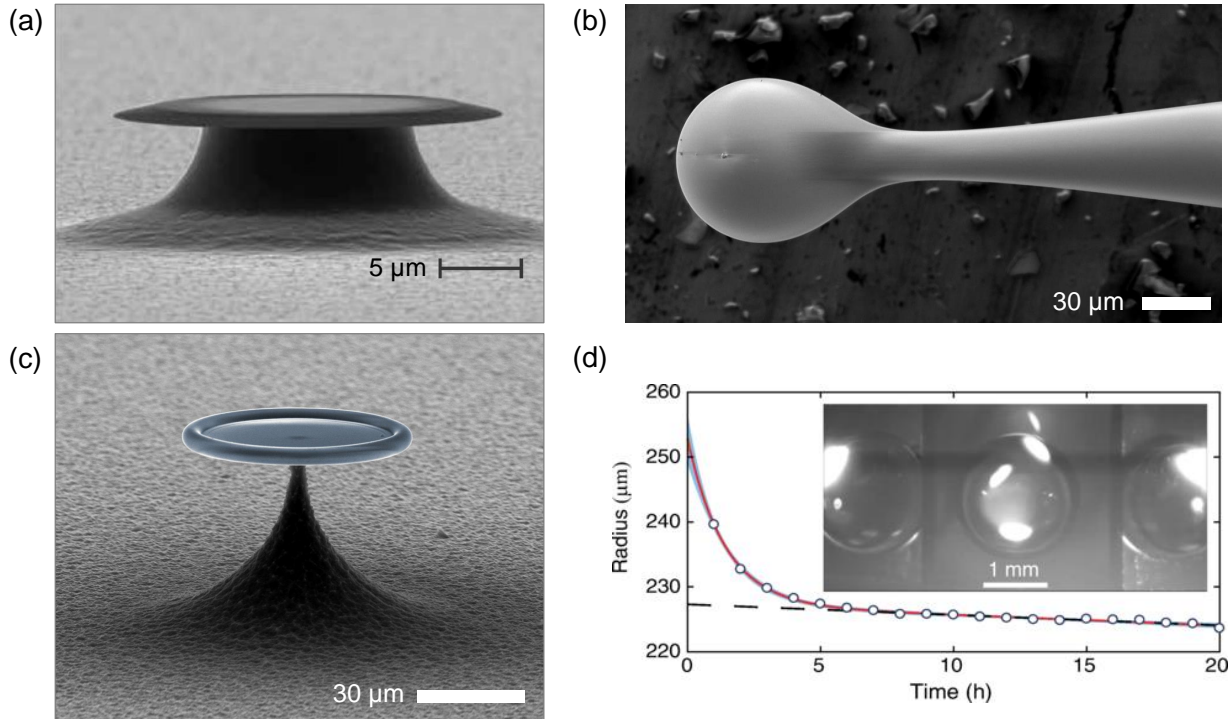


Fig. 3.4: (a) SEM image of an on-chip micro-disk resonator used to study Brillouin scattering in superfluid helium thin-films — taken from [6]. (b) SEM image of a silica micro-sphere formed through surface tension after heating a tapered silica tele-com optical fibre above its melting temperature, forming a near-atomically smooth surface (artefact in image is dust) — taken from [7]. (c) False colour SEM image of a silica-on-silicon micro-toroidal device, where the silica toroid has been rendered blue — taken from [8]. (d) Magnetically levitated superfluid helium droplets that support high finesse whispering gallery modes — taken from [9].

using a central ‘pedestal’, isolating the confined light to the edge with minimal scattering pathways. Variations can be made to this, such as seen in Fig. 3.4 (a), where the edge of the disk is bevelled, confining the optical mode more strongly within the substrate. Geometric modifications to these can be made as well, such as the design of a ‘micro-annulus’, which is of particular importance to the work presented in this report. Micro-annulus resonators take the form of a micro-disk, with material removed in the centre of the disk to form an outer annulus or ‘ring’, attached to a central disk with small ‘tethers’ (see Chapters 4 and 5). Silica micro-spheres are near-atomically smooth resonators, which have been used to demonstrate ultrastrong dynamical backaction in a superfluid helium thin-films [7, 30]. These devices provided a unique platform to superfluid helium in a geometry that approximates a shell, enabling thin-film third sound regimes of superfluid helium investigations with a high degree of control. These spheres are particularly unique for the study of non-linear hydrodynamics in 2D thin-film superfluid helium. Silica micro-toroids combine the atomic smoothness of micro-sphere resonators with disk-like geometry akin to micro-disks. These are formed through laser heating of a silica micro-disk, which through surface tension of

the melted glass forms a toroid-like at the circumference. These devices have been shown great success in superfluid helium laser control, and have been used to study coherently evolving vortex clusters in 2D superfluid helium thin-films [8, 41, 42]. Though in the regime of bulk fluid and first sound, magnetically levitated droplets of superfluid helium are a novel platform that supports whispering gallery modes. As an isolated sample, surface tension of the helium droplets induce particularly uniform spherical symmetry. These droplets offer a unique method in studying superfluid helium dynamics that may benefit from the lack of substrate, such as sound or roton investigations [9, 36].

4

Angular vortex generators

Previous investigations of quantised circulation in superfluid helium make use of rotating experimental apparatuses to induce circulation by varying the angular frequency of the entire experiment. These investigations mount an entire cryostat on a frame and is rotated by a motor and several revolutions per second. This includes the work conducted in observing the quantisation of circulation in bulk superfluid helium [38]. These experiments are limited in several aspects such as rotation speed, measurement schemes, sample sizes, and particularly the ability to conduct many experiments in a short time period. Superfluid optomechanics and integrated superfluids circuits are a promising platform to translate these past experiments onto a stationary chip by engineering devices that ‘inject’ circulation through optical control. Past work on quasi-2D superfluid helium thin-films using micro-toroid resonators have investigated this idea successfully, acoustically detecting net circulation — though not single quanta of circulation [8]. Devices used in this work lacked the ability to direct superflow angularly, and in controlling the generation of vortices. This chapter will outline the investigation of optimising ‘angular vortex generators’ (AVG) for superfluid optomechanics through numerical simulations. The basic design principles of these devices will be discussed, followed by discussion of understanding relevant superfluid vortex dynamics in these geometries. This work is motivated by the aim of implementing these devices into experiment, progressing towards detection of single quanta of circulation in 2D superfluid helium.

4.1 Basic principles of an AVG

An angular vortex generator (AVG) is a novel photonic device design based on micro-annulus whispering gallery mode resonators. The intended purpose of these devices is to engineer angular flow of superfluid through optical laser manipulation using optomechanical techniques in an otherwise stationary environment. A basic design involves three features; a central disk, a ‘connecting arm’, and an outer annulus (ring). These pedestal-based devices make

use of localised laser-heating induced evaporation of a WGM to drive flow from a thermal bath of superfluid [41], connected to the central disk, through the connecting arm, and into the outer annulus.

Designing asymmetries into the connecting arm allows for conversion of the lateral momentum of incident mass into angular momentum into the outer annulus. Additionally, the narrow channel that is the connecting arm acts as a vortex nucleation site under sufficient flow velocities — a basic AVG design can be found in Fig. 4.1. The following will cover understanding these concepts in greater detail, with emphasis placed on optimising the use of AVGs for induced net quantised circulation.

4.2 Computational investigation of superfluid helium dynamics in integrated photonic devices

4.2.1 Potential flow theory

Localised laser induced evaporation of a superfluid helium thin-film coating a micro-cavity resonator pushes the system into a state for which the particle number is less in the cavity than its surrounding ‘thermal mass’ reservoir. Understanding the steady state behaviour of this flow is a useful first step towards engineering superfluid photonic circuits. In the case of AVGs, or WGM resonators in general, this chemical potential imbalance occurs between the guided WGM and the pedestal — which connects the film to a much larger volume of superfluid helium in thermal equilibrium. This causes a flow up the pedestal, towards the optical mode, replenishing the evaporated superfluid. In the case of AVGs, this flow is designed to be directed through arms that ‘inject’ angular momentum into the outer annulus. Classical intuition would suggest that a narrow channel would see the velocity of the fluid increase, and under the right conditions, ‘turbulent’ or ‘chaotic’ behaviour may occur as the fluid enters the annulus, where the bulk velocity of the fluid is much lower. This intuition, for the most part, is correct, with some slight nuances one might prepare for when dealing with quantum systems. Potential flow theory is a very useful method in modelling steady state flows of fluids like this. Making an analogy to electrostatics, the evaporation and replenishment of particles in a fluid function as point- or boundary-like sources and sinks of charge, with the resultant electric potential stream lines describing the velocity field of the fluid. For AVGs, two loops of line charge can be applied as the source and sink of the superfluid. Setting the evaporation and replenishment regions as different electrical potentials, the calculated electric field lines become the streamlines of the fluid (after appropriate normalisation).

Solving the electric *potential* of these systems for the *flow* of a fluid is an electrostatics problem comfortably solved using finite element analysis (FEM) methods with appropriate computational software and/or packages. Fig. 4.1 is an example of solving this problem for a basic AVG design using the FEM ‘multi-physics’ package COMSOL. Here we see that our classical intuition qualitatively replicates the resultant steady-state flow field quite well. Noting a normalised scale, the magnitude of the velocity at the ‘injection site’ is significantly larger than anywhere else in the domain. This is expected from the conservation of mass in

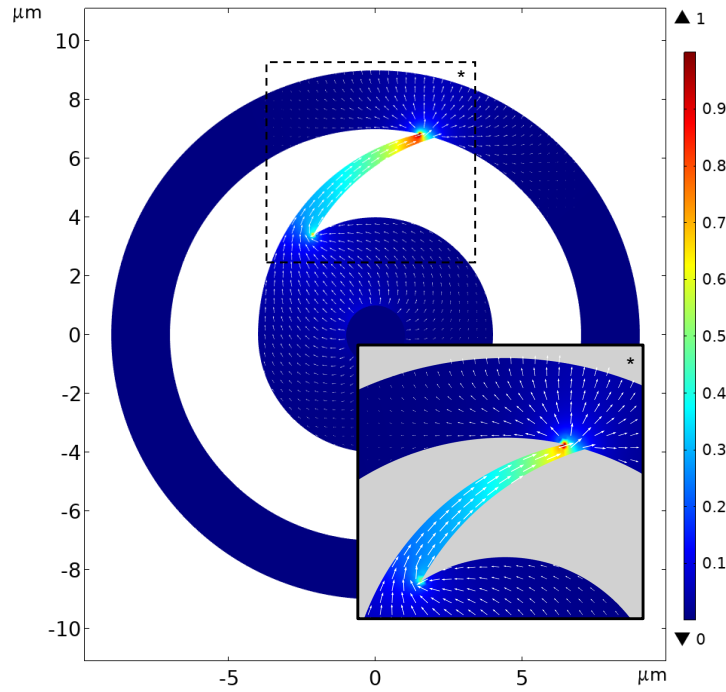


Fig. 4.1: Potential flow theory modelling of superfluid velocity streamlines in an angular vortex generator under laser-induced evaporation of superfluid helium along whispering gallery mode. Normalised velocity field depicts increase fluid velocity in regions of constricted flow, as per a classical intuition using Bernoulli’s principle for incompressible flow.

an incompressible flow (c.f. Bernoulli’s equation). Moreover, this flow is directed into the annulus as predicted, where the velocity of the fluid drops off drastically. These regions of large velocity gradients are studied extensively in many areas of fluid dynamics. In the case of superfluids, the most important phenomenon to consider here is Landau’s criterion for the critical velocity of the superfluid [51]. It is above this critical velocity that a superfluid will see dissipative effects through the elementary excitations associated with the normal fluid fraction of the system. These excitations of normal fluid enable point-like quanta of circulation about a topological defect — a superfluid vortex. Many investigations of quantum turbulence in superfluid rely on vortices and a phenomenon often described as a ‘mutual friction’, which acts as an effective viscosity in an otherwise inviscid fluid [52]. This effect is critical in enabling turbulent dynamics, and the importance of vortices in superfluid dynamics cannot be overstated. With the nature of many relevant mechanisms still proving to be contentious, there is much interest in studying vortex nucleation, annihilation, small and large vortex number dynamics. The nature of the geometry at the injection site, i.e. an abrupt change in cross-sectional area, leads to the critical velocity entering the annulus is substantially lower than through the arm. This leads to the possibility of the incident fluid having sufficient kinetic energy to begin nucleating vortices, and under continuous flow, ‘streets of vortices’ [51, 53]. Upon closer inspection of Fig. 4.1, a local velocity hot spot can be seen where the injection arm is incident on the central disk. This is an important point to consider, among many, in investigating device geometries in optimising reliably predicting

and controlling the generation of vortices.

Though this model provides incredibly useful preliminary knowledge, the actual dynamics of superfluids is far more complicated. As discussed, nucleation of vortices is one phenomenon unaccounted for, but we are also still in the dark when it comes to physics like sound waves, energy dissipation (for finite temperature systems), and namely quantised circulation. The effect of various geometric features of these devices on the formation of net quantised circulation can be more thoroughly investigated with the Gross-Pitaevskii simulation, where much of the physics missing from potential flow theory modelling is addressed.

4.2.2 Gross-Pitaevskii simulations

Single quanta of circulation in 2D superfluid helium films — even in very small volumetric regimes and precision optomechanics — will lead to only tiny perturbations in measured optical signals. Searching for single quanta of circulation in 2D superfluid helium thin-films is akin to searching for a straw coloured needle in a hay stack, but you’re not sure if there is a needle in there to begin with. Understanding driven and free evolutions of these modelled systems will provide incredibly valuable qualitative understanding of the possible dynamics to be observed in experimental investigations. Much work conducted in superfluid optomechanics involves both continuous and pulsed laser power operations. Often combinations of both are used to initialise dynamics over a pulse, followed by continuous measurement. Being able to computationally model the response of a superfluid to these control operations in AVG devices would prove to be invaluable in experimental investigations.

Building upon the intuition from potential flow theory, exploring possible device designs with the 2D Gross-Pitaevskii equation was conducted. This involved modelling device geometries and inducing flows analogous to what could be achieved by exploiting the laser-induced evaporation of the superfluid along the optical mode. The designs were based off of micro-disk third-sound resonators for thin-film superfluid optomechanics investigated in past works [8]. Fabrication processes needed to make these devices were carefully considered; an overview can be found in Sec 5.1. Many geometries were investigated to optimise the transfer of linear momentum to angular momentum, and hence emergence of quantised circulation. Briefly speaking, each of the investigated designs were comparatively assessed on the rate of vortex generation (with respect to drive strengths), under the consideration of preferential flow around the devices annulus — a critical phenomenon in generating net circulation.

The Gross-Pitaevskii equations works under many assumptions that are not necessarily valid for superfluid helium, a dense and relatively strongly interacting bose liquid, and some of these are discussed in the following sections. Despite many limitations of replicating experiment through simulation, the qualitative understanding of the superfluid dynamics remains mostly unaffected, leaving a wealth of physics to be investigated for AVGs and other integrated superfluid photonic devices.

The damped GPE

The novelty of AVG geometries compared to other work involving GPE modelling requires several unique considerations. Moreover, the dynamics of interest involve continuous and

localised driving of the fluid for, potentially, significantly long time scales. The Gross-Pitaevskii equation is well described in literature in modelling superfluids, and in the zero temperature limit, the equation describing the evolution of the macroscopic wavefunction can be described by

$$i\hbar\partial_t\Psi(\mathbf{r},t)=\left(-\frac{\hbar^2}{2m}\nabla^2+V(\mathbf{r})+g|\Psi(\mathbf{r},t)|^2-\mu(\mathbf{r})\right)\Psi(\mathbf{r},t), \quad (4.1)$$

where $V(\mathbf{r})$ is an external spatially dependent potential, $\mu(\mathbf{r})$ is the chemical potential, and g is a two-boson interaction strength [51, 54]. For our case of photonic devices, V will play the role of the van der Waals interactions responsible for confining superfluid helium films to on-chip devices [13]. We can approximate the physically three-dimensional devices as strictly two-dimensional, confining superfluid to the potential well V . In our case, V and μ do not explicitly depend on time, but physically they could enable observations of transient effects arising from laser pulses or optomechanical feedback interactions. This approximation is a limitation to the range of dynamics we can observe computationally compared to experiment. For example, after a generation of a vortex pair of opposite sign, one may be transported to the ‘other side’ of the device, resulting in very different velocity fields and a net circulation. These sort of dynamics are missing in these computational approaches, but are critical in understanding the true dynamics of superfluid photonic devices.

The GPE is often not analytically solvable, and numerical methods are needed to investigate most dynamics of interest. It is often convenient to dimensionally reduce parameters when solving problems like this. For the GPE, this is often done using the ‘healing length’ ξ , which describes the typical characteristic length scale for which excitations in the fluid will decay. The value of the healing length is system-dependent, and is often related to the interaction strength g . In dilute weakly interacting superfluids like BECs, the healing length may be as big as a micron, but as small as an angstrom for helium-4, a dense, strongly interacting superfluid. Equating interaction energy and kinetic energy, the healing length can be described by $\xi = \hbar/\sqrt{2m\rho_0 g}$, where ρ_0 is the bulk density of the superfluid — the normalisation coefficient of a uniform wavefunction (see Eq. 2.3) [54]. Rescaling our coordinates to $\bar{t} = t/t_0$ and $\bar{x} = x/\xi$, with $t_0 = m\xi^2/\hbar$, and writing the interaction strength as $g = \hbar^2/2m\rho_0\xi^2$, Eq. 4.1 can be made dimensionless:

$$i\frac{\partial\Psi}{\partial\bar{t}}=\left(-\frac{1}{2}\nabla^2+V+|\Psi|^2-\mu\right)\Psi, \quad (4.2)$$

where Ψ has been relabelled from $\bar{\Psi}$ after implementing $\bar{\Psi} = \Psi/\sqrt{\xi}$, and $\hbar = m = \rho_0 = 1$. So far we have described a superfluid in the zero temperature limit, which does not paint the best picture in understanding experimental dynamics. To account for this, we make use of the *damped* GPE (or ‘dGPE’)

$$i\frac{\partial\Psi}{\partial\bar{t}}=(1-i\gamma)\left(-\frac{1}{2}\nabla^2+V+|\Psi|^2-\mu\right)\Psi, \quad (4.3)$$

where γ governs the strength of damping. In superfluid helium thin-films, we need to consider the effects of damping interactions with the normal fluid fraction of the condensate. This

stems from the finite temperature nature of the system, but also interactions with the optical field which can evaporate helium atoms. Here laser heating introduces thermal interactions in the film, which in combination with locally increased normal fluid fractions and the fountain pressure effect, leads to significant local damping of film. The dGPE is well studied and used extensively in modelling BECs and superfluid dynamics, however, as previously mentioned, the novel geometry of AVGs and intended experimental implementation requires some further extensions to better describe the evolution of the superfluid using optical control [53, 55–57].

A sink-source model for the dGPE

In order to simulate driven flow in the superfluid — analogous to laser induced evaporation — a ‘sink-source’ approach can be used. This involves modifying the dGPE by implementing spatially varying chemical potential terms to approximate the evaporation (sink) and particle reservoirs (source). For AVGs, evaporation of the superfluid is localised to the tightly confined WGM along the outer circumference of the annulus, and the fluid reservoir being concentric to the central pedestal of this micro-annulus geometry. A particle number imbalance (a chemical potential difference) between these two regions would expectantly lead to a velocity field similar to that seen in Fig. 4.1. However, simply initialising a system this way would lead to evolution towards equilibrium of chemical potentials. To enable sustained driving, the chemical potential delta needs to be constant for all time, mimicking the physical evaporation of particles along the circumference, and ongoing replenishing flow.

This can be achieved phenomenologically with an additional chemical potential term μ_d to Eq. 4.3 — equivalent to the stochastic projected GPE (SPGPE) when excluding thermal noise [56, 58]. This produces a modified dGPE of the form

$$i\frac{\partial\Psi}{\partial t} = (1 - i\gamma) \left(-\frac{1}{2}\nabla^2 + V + |\Psi|^2 - \mu - \mu_d \right) \Psi. \quad (4.4)$$

where $\mu_d(x, y)$ is a spatially dependent effective ‘driving’ chemical potential, which μ can be absorbed into without loss of generality. To form an intuition of this modification, μ_d can be considered a kind of dial, governing the flow of fluid in some region (assuming spatial non-uniformity of μ_d). When $\mu_d = 0$, it is clear that we reduce back down to the standard GPE. However, setting $\mu_d > 0$, we begin to ‘inject’ some additional proportion of the wavefunction in a region onto itself, damped by γ . This of course is not generally normalisation-conserving on its own, and the total density $|\Psi|^2$ will continue to change for constant $|\mu_d|$. Similarly, $\mu_d < 0$ will ‘evaporate’ some proportion of the wavefunction. Constructing the spatial profile of μ_d carefully allows us to maintain steady state flow with the mass of the system constant in time, i.e. $\dot{m}_{\text{system}} = 0$. To do this, the divergence of mass flux of the superfluid must be zero, which implies

$$\iint \mu_d(x, y) dx dy = 0. \quad (4.5)$$

Under this constraint, Eq. 4.4 can be used to model steady state flow upon laser heating of an optical cavity, specifically an AVG. However, this form of the GPE is far more versatile than this use case, with applications in modelling superfluid dynamics in geometries of non-global driven flow.

Computational limitations of simulated device dimensions

What remains to be discussed are the limitations of computational domain size. It is important to note that, experimentally, the size of a device is limited by the precision of fabrication, sensing equipment, and through WGM ‘bending losses’ when the wavelength of confined light is large compared to the radius of the device. Considering this led to determining a device radius of $\sim 10 \mu\text{m}$. This is very small. Past work has seen success in investigating similar devices of $30 \mu\text{m}$ radii (see Fig. 3.4) [8]. Eq. 4.4 is spatially characterised by the healing length, which by many definitions for superfluid helium-4 is on the order of an angstrom. One such definition is the radial distance from a singly charged vortex core for which the kinetic energy surpasses the thermal energy of the transition temperature ($\varepsilon_c = k_B T_c$), which is approximately 2.5 \AA . This fact greatly affects the ability to model a one-to-one scale device. A domain size of even $L = 1 \mu\text{m}$ would require 10,000 grid points for one dimension of \bar{x} with the case of $d\bar{x} = 1$. Note that this spatial step size is really the upper limit of what can be used when observing vortex dynamics (objects of size not much larger than this) is desired. Therefore, the simulation domain was restricted to a reasonable scale of 450×450 grid points, with $d\bar{x} = \xi = 1$. This scaling places the simulation at several orders of magnitude smaller than the planned devices. However, the resulting dynamics are still useful in investigating the qualitative behaviour of device designs — an incredibly valuable resource in many facets of experimental implementation. The final relevant approximation is the shape and profile of μ_d . For simplicity, the spatial profiles of these parameters were hard-walled, with minor Gaussian smoothing of the boundaries. Though this is not necessarily physical, it serves as a useful approximation to initiate a basic superflow. The source ($\mu_d > 0$) and sink ($\mu_d < 0$) were positioned around a central pedestal and circumference of the annulus, respectively. An approximate penetration depth of the optical mode along the edge of a resonator was taken as the radial width for $\mu_d < 0$ as $\sim 1 \mu\text{m}$, which was scaled appropriately in units of \bar{x} . The resulting ‘loss area’ was used to enforce the size of the source as an annulus around a central pedestal of radius $\sim 1 \mu\text{m}$, adhering to Eq. 4.5. It should be noted that the inclusion, or rather removal, of the occupied space by the pedestal does result in a geometry of genus 2 (a two-holed torus). This allows for locked circulation about the pedestal [8]. This is not physical in the sense of experiment, but is also unlikely to occur by the nature of the direction of the driven fluid. Most importantly this would not affect the qualitative analysis of the simulations, where we focus here on the engineered defect formed by the annulus.

Computational methods overview

Initialising a given design with its relevant parameters (V and μ_d) was done using MATLAB. The solving of Eq. 4.4 was achieved using XMDS2 and its 4th/5th order adaptive Runge-Kutta method (ARK45) in combination with spectral methods [59]. Evolving to time scales of upwards of $\bar{t} = 10,000$ is easily accessible, allowing observation of long life-time dynamics. Though this is the case, the implementation of Eq. 4.4 to drive the system is often only required on time scales of no more than $\bar{t} = 2,000$, though this is dependent on the magnitude of the gradient of the driving term μ_d .

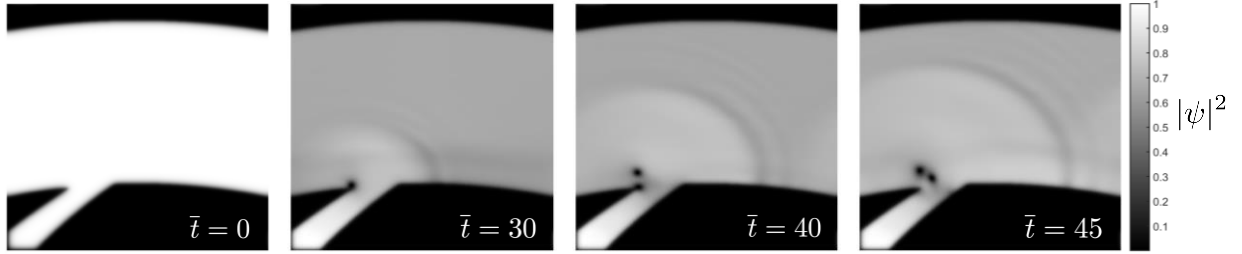


Fig. 4.2: Initial generation of a like-signed (positively signed) vortex cluster at superfluid velocities slightly above the critical velocity v_c . Evolution of longer times sees a (negatively signed) cluster form, originating from the ‘corner’ shallower break angle of the injecting arm incident on the outer ring, as predicted from potential flow modelling (see Fig. 4.1). Continued evolution sees repeated oscillation of these vortex streets, with larger driving strengths leading to smaller cluster sizes i.e. vortex-antivortex pair production.

Overview of investigated design parameters

In overview, superflow through a narrowed (connecting arm) channel can lead to the fluid moving faster than the critical velocity v_c at the interface between the arm and the outer annulus. At velocities slightly above the critical velocity, clusters of same-signed vortices form as ‘vortex streets’, and are injected into the annulus [53]. The initial generation of these vortex streets can be seen in Fig. 4.2, where a difference in μ_d is applied between the arm and the edge of the annulus (section) for $\bar{t} > 0$. Larger velocities and longer time scales display two vortex streets at each ‘corner’ of the injection site. Here, vortex nucleation in each street occurs almost simultaneously as a generation of an ‘vortex-antivortex’ pair of opposite sign. In reference to Fig. 4.2, the left vortices will be called ‘positively’ signed, with the phase increasing in the anti-clockwise direction, and vice versa for the right corner, as discussed further in the following section (see Fig.4.3).

Investigation of various design parameters focused on understanding the role that each feature plays in inducing a net circulation. Moreover, effort was placed into optimising these features such that minimal driving strength and driving times are needed for consistent formation of locked circulation to the AVG, whilst maintain a feasible level of control in the final charge number κ of the circulation.

Mechanism of locked circulation in AVG GPE simulations

The following is a qualitative understanding built upon the investigation of many design iterations, driving strengths, driving times, damping strengths, and free evolution of vortex dynamics.

Given enough time and under appropriate laser heating conditions, a net difference in signed vortices can form, contributing a net circulation in the fluid. This is a consequence of the damping that occurs in the regions of $\mu_d \neq 0$, particularly along the ‘heated’ edge of the device where $\mu_d < 0$. Consider a vortex pair generated at the interface of the arm

and ring (the injection site), with directed flow in the clockwise direction. These pairs form in opposite sign, travelling in the direction where their velocity fields add together — just as vortices formed at the edges of a spoon moved through a cup of tea would travel. An important concept to convey here is the idea of an ‘image vortex’, which is an intuitive picture that describes the velocity field of a single vortex changes as it approaches a boundary, like the wall of a potential [51, 54]. Image vortices are not physical, but describe how the velocity field is solved for a trapped condensate using the method of images — analogous to electrostatics. A positively charged vortex sitting at the edge of a disk trap ‘sees’ a velocity field equivalent to if an equidistant and opposite signed image vortex were positioned on the other side of the potential barrier. The vortex in the trap would then follow the resulting flow field, and begin to orbit anti-clockwise around the trap, or rather, along the wall with its image. Returning to our injected vortex pair travelling around the ring, the clockwise background flow places the positively signed vortex on the ‘wrong’ side of the ring, where moving with its image would be against the background, and similarly for the negatively signed vortex. This is energetically unfavourable and the vortices begin to ‘mix’, and after enough time they switch sides of the ring. At this point, the negatively signed vortex is now on the outer edge of the ring, where gentle damping — by artificial laser heating ($\mu_d < 0$) — may cause it to lose energy and annihilate at the boundary (with its image). This results in the negatively signed quanta of circulation of the annihilated vortex becoming ‘locked’ to the device. This leaves just the positively signed vortex on the inside edge of the ring. With a sufficient number of initial vortices upon driving the system, free-evolution (with gentle damping at the edge) should result in a net difference in signed vortices given enough time. In the case of clockwise background flow, positively signed vortices dominate and the annihilated, negatively signed vortices contribute to a total locked circulation.

Locked circulation emerges as a continuous loop or ‘winding’ of the phase parameter Φ from $-\pi$ to π about the central topological defect (see Eq. 2.2). This is equivalent to the emergence of a net velocity flowing around the ring since the gradient of the phase parameter is the superfluid velocity (see Eq. 2.5). The total number of locked quanta of circulation, κ , can easily be counted, where every period of 2π adds one circulation to the total. Diagrammatic examples of a point vortex phase winding and the locked circulation we are interested in can be found in Fig. 4.3. As a point of context, topological vortices are often of circulation $\kappa = 1$, with a larger ‘charge’ configuration becoming an increasingly less energetically favourable state [13]. This is a consequence of the small core size of topological vortices, but larger defects enable larger values of κ . The kinetic energy associated with these phase windings drops off as $1/r$, and so a larger core means there is less rotational mass, and hence less kinetic energy per κ , leading to larger numbers of circulation being energetically accessible.

In these simulations, devices were modelled as hard-walled traps, and the effects of ‘softer’ walls was not investigated. However, experimentally these devices have no ‘walls’, and the superfluid coats the devices continuously. In a sense, the edges of the device where the coated superfluid ‘curves over’ may be more akin to soft wall potentials. Past work on vortex pinning mechanisms for obstacles in superfluid thin-films have shown that the minimum background velocity to unpin a vortex increases with the effective potential strength of the obstacle [60]. The continuous coating of superfluid helium in these devices may then have

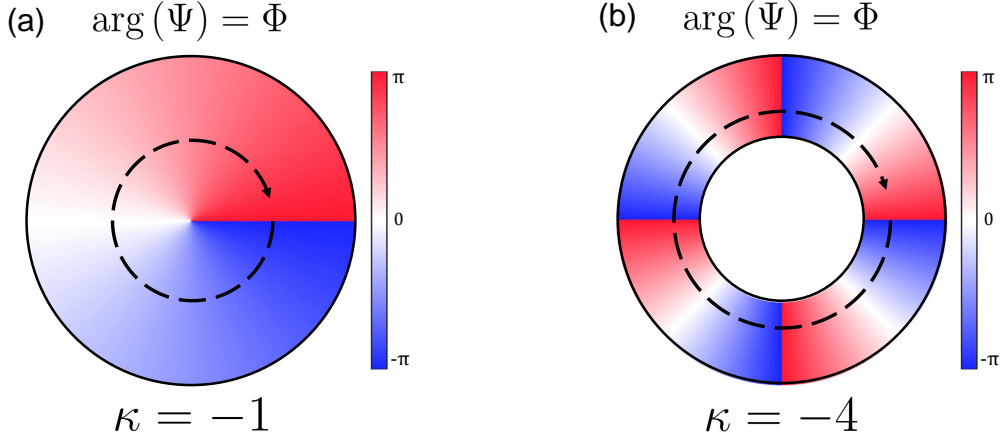


Fig. 4.3: Phase windings diagram of lock circulation in a superfluid. (a) A single ‘charge’ of circulation (one period of 2π phase) around a point defect — a quantum vortex. (b) A multi-charge circulation around a larger engineered topological defect, similar to the form discussed in the geometry of angular vortex generators.

a relatively small effective potential strength as a defect. Considering this, it may be the case that the persistent superflow associated with net circulation will lead to unpinning of the locked circulation. The specifics of this problem are complicated dramatically by the three-dimensional geometry on which the two-dimensional surface lives. Nevertheless, these unpinning (and pinning) mechanisms are fundamental in the emergent physics of superfluid vortex dynamics.

The optimisation of achieving locked quanta of circulation in AVGs through the process described above was investigated using many different designs. Each design was used to move towards maximising the number of locked circulation achievable in short time scales under modest driving strengths. Many different design parameters, dimensions, and modifications were investigated. As one might expect, the majority of these parameters are critical in effectively generating locked circulation, with many needing to be in some optimal regime. For example, the cross-sectional width of a connecting arm plays a large roll in accelerating the fluid past the critical velocity to generate vortices. If the width is too large, then very large driving terms are needed to generate vortices, which is not ideal for experimental implementation, where minimal heating is preferable. On the other hand, if the width is too narrow, many vortices are generated, but bulk mass flow is limited, which is essential in directing the vortices in a preferred direction. Furthermore, as one could intuit from a classical perspective, having the injecting arm arrive at a angle normal to the annulus would result in symmetric vortex distributions without biasing the system towards a net circulation. The free dynamics of several systems were investigated, with an initial generation of vortices, and evolution under localised damping at the edge of the AVG, mimicking the experimental optical measurement. This leads to persistent flow around the device, with vortices occasionally dissipating at the boundaries by the mechanisms described previously.

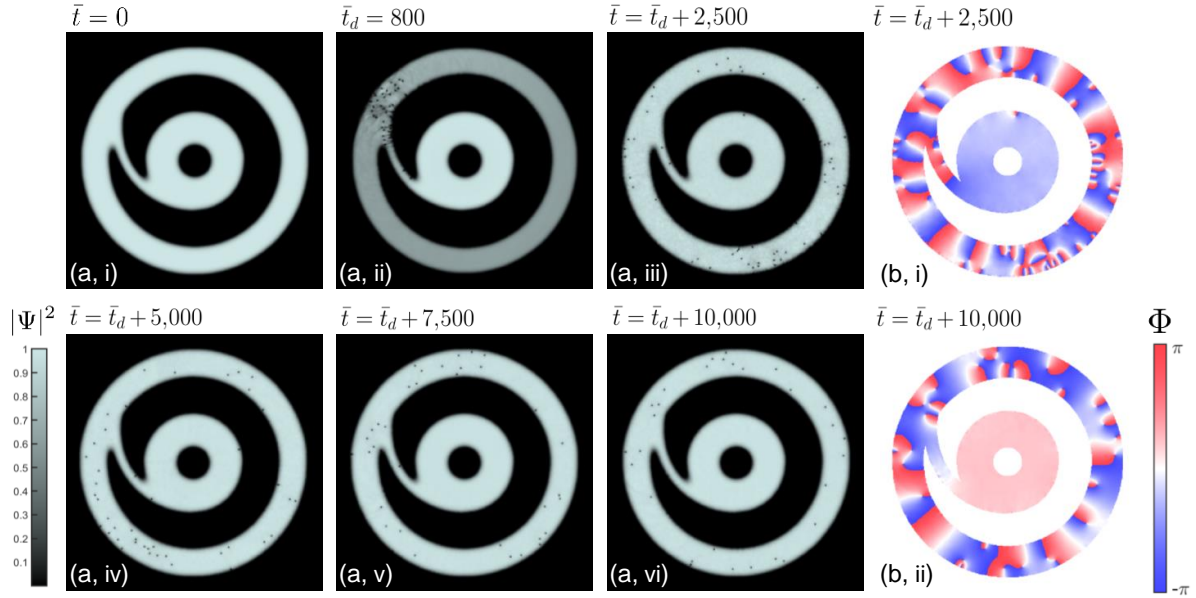


Fig. 4.4: **(a)** Wavefunction density ($|\Psi|^2$) snap shots of ‘free dynamics’ after an initial drive of constant strength from the ground state **(a, i)** until $\bar{t} = 8,000$ **(a, ii)**. Localised areas of vanishing density are topological quantised vortices. A small amount of damping is localised by an approximated penetration depth of guided light at 1550 nm in the projected AVG photonic device sizes. **(b)** Wavefunction phase snap shots across simulation time. Closed loops of integer steps of 2π of the phase around the central defect is a representation of quantised circulation, whilst loops around point defects are vortices. At $\bar{t} = 2,500$, the number of vortices are $n^+ = 34$ and $n^- = 24$ for positively and negatively signed vortices, respectively. At longer time scales vortices continue to mix and annihilate. At $\bar{t} = 10,000$, $n^+ = 17$ and $n^- = 10$, where several κ of locked circulation can be observed around the annulus (see Fig. 4.3).

Long time scale dynamics and controlling net circulation

Experimentally controlling the induced locked circulation number is key to identifying single quanta of circulation. To investigate this numerically, Eq. 4.4 was used to drive a device for some amount of time, before evolving the system with the driving turned ‘off’ to observe free dynamics of mixing and vortex annihilation processes. Free evolution refers to switching off the fluid driving, which is equivalent to evolving the system under a standard GPE. However, as discussed, the laser-heating and subsequent damping at the edge of the annulus is critical in controlling the formation of locked circulation. As such, a small amount of damping localised to the edge of the annulus was added in most simulations of this numerical ‘experiment’, an example of which is displayed in Fig. 4.4. Success in producing locked circulation prompts the investigation of how the system responds to varying strengths and durations of driving. Insufficient driving strengths, or equivalently connecting arms of excessive width, result in driven systems that achieve equilibrium without the generation of vortices or net circulation. With this it can be identified that the nucleation of vortices is essential in inducing angular persistent flow. Conversely, connecting arms of overly narrow width lead to sufficient vortex generation, but lack the bulk mass flow that initially ‘pushes’

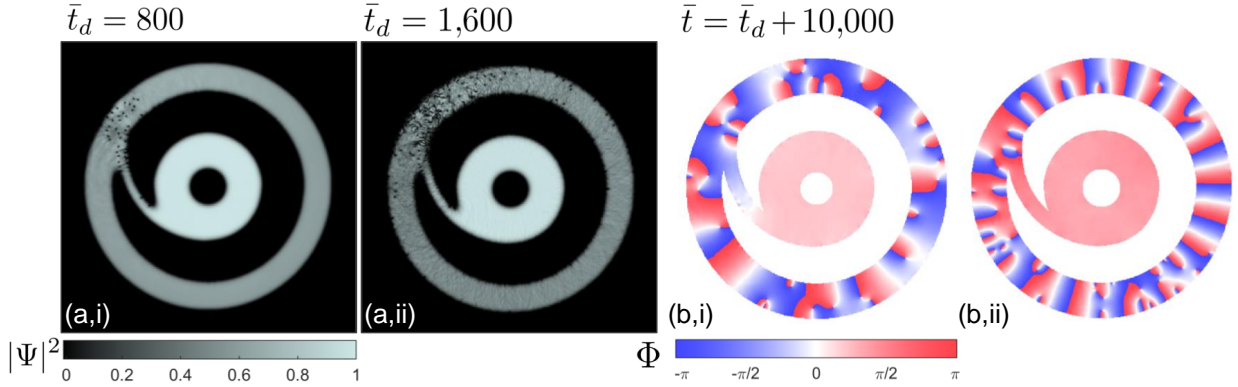


Fig. 4.5: **(a)** Comparison of different initial driving durations, with the wavefunction densities upon evolving the un-driven system under gentle damping at the edge of the annulus. **(b)** The respective systems' phase profile after 10,000 time steps of evolution. As per Fig. 4.4, **(b,i)** displays the vortex numbers $n^+ = 17$ and $n^- = 10$, though the longer initial drive **(b,ii)** leads to $n^+ = n^- = 19$, with a significantly larger value of locked κ observed around the annulus. It should be noted here that the net locked circulation is resultant of vortices annihilating with their images, which is not necessarily depicted through the presence of a net difference of signed vortex number.

the vortices around the annulus, which leads to symmetric mixing (no net circulation). Excessive generation of vortices, through large driving strengths and durations, will lead to a system of large kinetic energy, in which it takes longer to see preferential annihilation of vortices, given unchanged damping strengths. However, modest variation of driving periods/strengths enables control of the induced circulation in reasonable time scales. With the increased number of vortices and subsequent net difference of signed vortex annihilation events at the boundary, longer/stronger driving leads to larger numbers of locked circulation. This effect is demonstrated in Fig. 4.5, where a doubled initial driving duration to Fig. 4.4 leads to larger net circulation under the equivalent time duration of free evolution.

The intuition and understanding of these relevant design features are essential in designing viable integrated superfluid photonic devices for the observation of single quanta of circulation in superfluid helium thin-films. Though this understanding is invaluable, as discussed in this section, this computational modelling has significant approximations that do not apply in experiment, namely the planar geometry with 'hard wall' boundaries. The transition into coated, rather than trapped, superfluid dynamics is far outside the scope of these methods, and experimental work using AVGs is needed to progress this understanding.

5

Device fabrication and experimental implementation

The plethora of angular vortex generators simulated with the Gross-Pitaevskii equation in Chapter 4 were used to select several designs to be fabricated and implemented experimentally. The following chapter will outline selected device designs and their implementation as integrated photonic devices. Moreover, design choices relating specifically to integrated photonic devices, basic overview of relevant fabrication processes, and device ‘characterisation’ will be discussed. Selected designs were drawn using the CAD software ‘KLayout’, which interfaces with the electron beam lithography (EBL) system at the Centre of Microscopy and Microanalysis (CMM) facilities located at UQ. Successfully fabricated devices are discussed, including their viability in superfluid experiments in the immediate future. Completion of clean room and fabrication training is not feasible in the time frame of this project, as such, the fabrication process of these devices was undertaken by PhD student N. Luu.

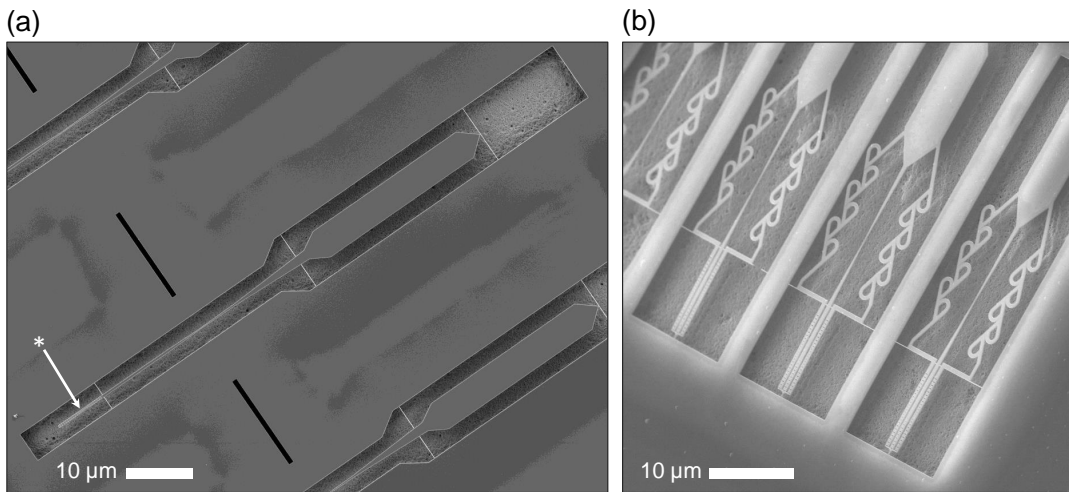


Fig. 5.1: **(a)** 1D photonic crystal ‘wave tank’ to study highly non-linear superfluid helium hydrodynamics. The optical cavity (see *) enables precision control and measurement of superfluid helium thin-films, providing a platform to study unique fluid physics at unprecedented wave size aspect ratios. **b** Superfluid helium ‘Tesla valves’ with precision control and measurement enabled by similar optical cavities in **(a)**, where two different resonant frequencies enable driving of ‘forward’ and ‘reverse’ valve directions. These complex geometries are a platform to study turbulence-dependent classical fluid phenomena in the quantum regime of superfluid helium, where quantum turbulence is not well understood by the characteristic lack of viscosity in superfluids.

5.1 Fabrication process overview

Before outlining the relevant photonic device design used in this project, the general process of the nanofabrication used to create them should be outlined. Nanofabrication is an extensively used process, which for integrated photonics enables an almost endless number of possible designs. The devices discussed in this work are relatively simple to fabricate compared to other works, relying only on a single active layer (with no metal electrodes for instance). However, optimising designs for implementation with superfluid helium optomechanics is not a trivial task. Angular vortex generators are a novel design in this field, but a multitude of complex and unique geometries are accessible with similar techniques (see Fig. 5.1). The following summarises the general process used in this work, and typical for pedestal micro-disk resonator devices:

Devices are fabricated from a ‘silicon on insulator’ (SOI) chip. These chips consist of three distinct layers, each of their own thickness; a 220 nm top layer of silicon, a 3 μm middle layer of silica, and a final 700 μm base layer of silicon. A layer of ‘resist’ is deposited on the surface of the chip, and electron beam lithography is used to pattern the desired device, removing selected areas of the coating. The exposed silicon surface is then etched using ICP-RIE (inductively coupled plasma-reactive ion etching), which selectively removes the top layer of silicon from the chip, leaving behind the flat device geometry that was coated in resist.

For these free-standing devices, further fabrication is needed to ‘release’ them from the silica layer underneath. Using appropriate etch rates and times, a pedestal-supported micro-disk device can be left behind after etching, along with a free-standing waveguide, supported by several narrow tethers. This additional step can be complicated, with the final diameter of the pedestal being difficult to control. The silica is selectively etched using HF vapour etching, with the etch rate being mostly governed by the temperature of the nanofabricated device positioned over the volatile HF vapour — lower temperature leads to a faster etch rate. Water is adsorbed to the device’s surface as a catalyst for the HF, and at lower temperatures, more water condenses on the chip, and hence more HF vapour can be catalysed.

5.2 Designing integrated photonic devices

5.2.1 Device dimensions and details

Four devices were selected for initial fabrication and experiment, varying from a basic device, labelled ‘d1’ (Control). The d1 design is axially symmetric with its injecting arm not taking the shape of an ‘arc’, but rather being incident normal to the outer annulus. The first variation of d1 is the addition of an arc of constant (circular) width to the arm, defining the design labelled ‘d2’. The third device ‘d3’ varies from d2 by implementation of a tapered arc (T-Arc), which narrows as it approached the outer annulus. The fourth design is a minor variation to d3 which includes an acoustic ‘damper’, labelled ‘d3(d)’, as a potential pathway to acoustically detect circulation through mode splitting (see Sec. 3.5). The dimensions of the three design geometries are collated in Tab. 5.1. These basic variations and intentionally simple features were chosen to serve as a platform to verify any findings throughout experimental investigation of superfluid helium circulation. The control device acts as a base line, and the two arc-like designs, d2 and d3, act roughly as (naïve) markers between two levels of vortex number generation and bulk fluid mass injection rate — fewer vortices and more mass for d2, and vice versa for d3 — see Fig. 5.8 for design images and Tab. 5.1 for relevant dimensions. The connection between the arc design and vortex generation is a concept discussed in Chapter 4. Larger superflow constriction at the injection site leads to greater superfluid velocity, in turn a faster rate of vortex generation — though at the cost of linear fluid momentum.

Parameter	d1 (Control)	d2 (Arc)	d3 (T-Arc)
	Dimension		
R_{disk}	5 μm	5 μm	5 μm
Ann. R_{out}	11 μm	11 μm	11 μm
Ann. R_{in}	8 μm	8 μm	8 μm
Arms	1	1	1
Arc	—	✓	✓
w_{arm}	2 μm	1.5 μm	0.7-1.5 μm^*
Tapered	—	—	✓
Arc R_{out}	—	8 μm	8 μm^*
Arc R_{in}	—	6.5 μm	8 μm^*

Tab. 5.1: Fabricated device design dimensions and features. *Tapered injecting arm design involves ‘subtraction’ of two eccentric disks of same (or different) radii, leading to injecting arm of non-constant width (see Fig. 5.2 and Fig. 5.8).

5.2.2 Implementation of on-chip optical coupling

The following will outline relevant integrated photonic components, and as a visual aid an example CAD drawing of an investigated device (d3) in Fig. 5.2. The most critical element of a WGM resonator is being able to couple to an optical mode located at the outer edge of the device. For the devices in this work, this was implemented through an evanescent coupling scheme through an on-chip ‘coupling waveguide’ [61–63]. This technique relies on the field propagating outside coupling waveguide to be near enough to an optical mode that (under the right conditions) it will ‘hop’ from the waveguide to the optical mode (i.e. evanescent coupling). The proportion of light coupled from the waveguide to the resonator is dependent on the frequency of light, refractive index of the material(s), and separation distance between the guided modes. The optical field is ‘critically coupled’ when the maximum amount of coupled light is achieved for a given frequency and refractive index, i.e. $|\mathcal{R}|^2 = 0$ (see Eq. 3.21).

An optimal separation distance can be determined through finite element modelling (FEM), such as the use of a software like COMSOL. In the interest of time for this project, several separation distances were investigated, positioned around known critical coupling distances for similarly sized devices in past work [8, 39, 41]. Experimentally, these on-chip waveguides are optically coupled to using a standard telecom silica optical fibre, the end of

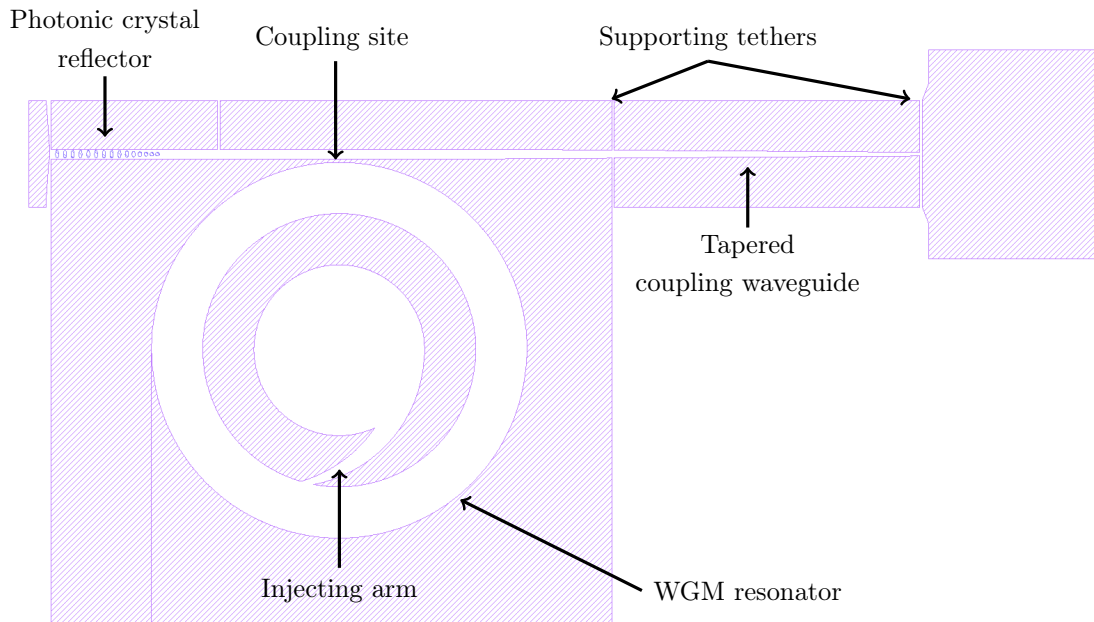


Fig. 5.2: Example CAD drawing of an investigated device design (d3) using KLayout.

which is adiabatically tapered [64, 65]. As such, a similar taper is integrated into the on-chip waveguide in order to couple the optical fibre to the waveguide, and hence the optical fibre to the device. Finally, the coupled light needs to be reflected back into the optical fibre, which is done by implementing an ‘optical mirror’ at the end of the waveguide, past the evanescent coupling site. An optical mirror was implemented as an array of elliptical holes in the waveguide. These act as a alternating stack of varying effective refractive indices, forming a 1D Bragg mirror which effectively reflects light. To minimise scattering losses in this process, the elliptical holes are preceded by several holes of decreasing eccentricity, starting with a circle. This ‘tapering’ of the optical mirrors acts like a graded refractive index, helping reduce optical losses.

These devices and coupling waveguides are mostly free-standing, with the AVG being supported by a pedestal formed by selectively etching the silica layer beneath it. However, this leaves the much smaller-dimensioned waveguide completely free-standing. At this scale, the ratio of the length to cross-sectional area for the waveguide can quickly become significant enough that slight internal stresses within the SOI wafer (relieved through the etching process) can buckle, bend, or even twist the waveguide. This is not ideal if it would occur near the coupling site of a device where efficient coupling can be the difference of a few 10’s of nanometres. This problem is typically solved by attaching tethers along the length of the waveguide, anchoring it to the bulk of the chip that — positioned far enough away to avoid scattering of guided light. These tethers can be scattering sites as well, and it is desirable to use the thinnest and fewest number of tethers feasibly possible to properly support the waveguide. Methods in optimising these tethers will be further discussed later in this chapter. Each fabrication process involved two identical chips, one for the sole purpose of experimental implementation, the other as a ‘sacrificial’ chip for SEM imaging. Simply transporting and handling a chip exposes it to the environment enough that incidental or

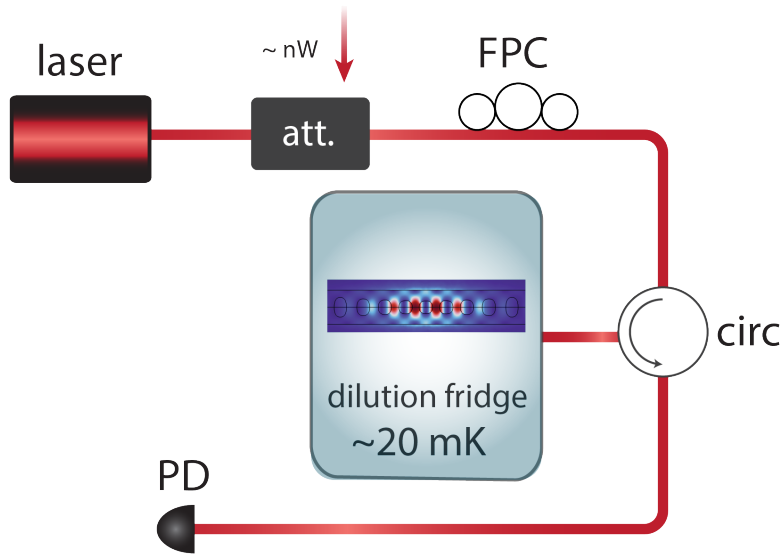


Fig. 5.3: General schematic of optical circuit used in characterisation, experimentation of integrated photonic devices for superfluid helium. Depicted photonic device implemented in the dilution refrigerator is a 1D photonic cavity, but through on-chip implementation, many different photonic devices are accessible for a given setup. An input laser is attenuated to nano-watt power levels and coupled to devices using a tapered optical fibre mounted to piezo-electric nano-adjusters. Figure provided by N. Luu.

unavoidable damage is very likely.

5.3 Characterisation of devices

5.3.1 Optical coupling and data acquisition

During and after the fabrication process, devices are checked for both efficient WG coupling and evidence of evanescent coupling to the WGM by the presence of optical resonances. This typically involves on-bench coupling to the WG with an optical circuit following the setup in Fig. 5.3. Successful coupling is often indicated by an oscillating optical reflection spectrum (see Fig. 5.5). This sort of reflection spectrum is a result of interference of the incoming and outgoing optical fields at the coupling site. Resonances are found by sweeping through a range of wavelengths (1500-1600 nm), and the presence of periodic Lorentzian-like dips (see Eq. 3.21) of amplitude larger than the noise floor are evidence that light is successfully being coupled into the WGM resonator, and the fabrication process was ‘successful’. An optical microscope and micro-adjustable mounts are used to align the devices’ tapered coupling waveguides with a tapered telecom-fibre (see Fig. 5.4). It is often the case that device resonances are polarisation dependent, and characterisation involves manipulating the polarisation of the fibre-guided light to search for resonant modes. This process is essential in determining if a problem occurred during the fabrication process. An example characterisation spectrum of coupling to a device is displayed in Fig. 5.5.

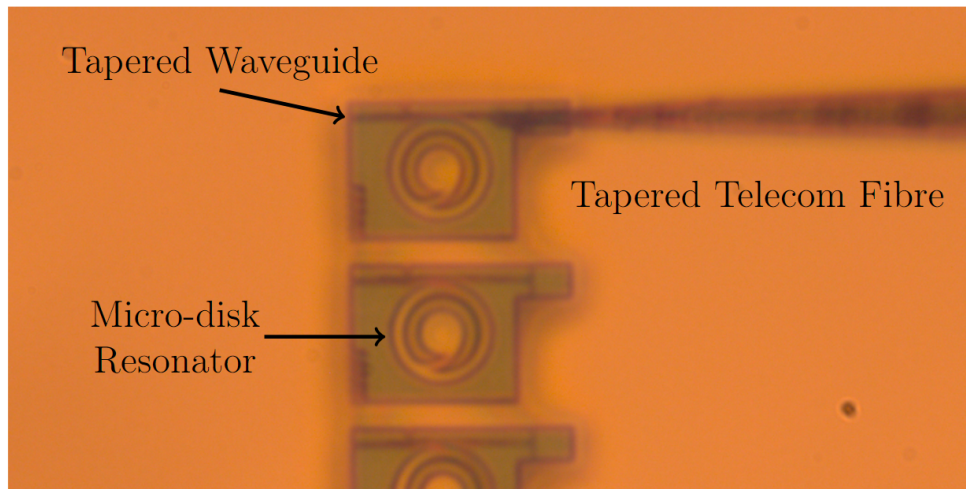


Fig. 5.4: Optical microscope image of coupling to fabricated devices, designed as outlined previously. The tip of a tapered optical fibre is aligned with the integrated tapered coupling waveguide, evanescently coupling light into the device. The incident light, now confined to the waveguide, travels towards the edge of the AVG, where evanescent coupling into the resonator may occur. Light that remains uncoupled to the resonator reflects off the 1D Bragg mirror, with the possibility to couple to the AVG again before evanescently coupling back into the tapered fibre — leading to a CCD photo detector.

Initial design and fabrication testing saw minimal success in achieving evanescent coupling between the on-chip waveguide and AVG devices. Additionally, despite observed resonances like Fig. 5.5 displaying particularly high loaded optical quality factors, the ‘contrast’ of any given resonance was particularly low. These facts indicated necessary improvements to device designs, focusing on coupling efficiency and between the AVG and the coupling waveguide.

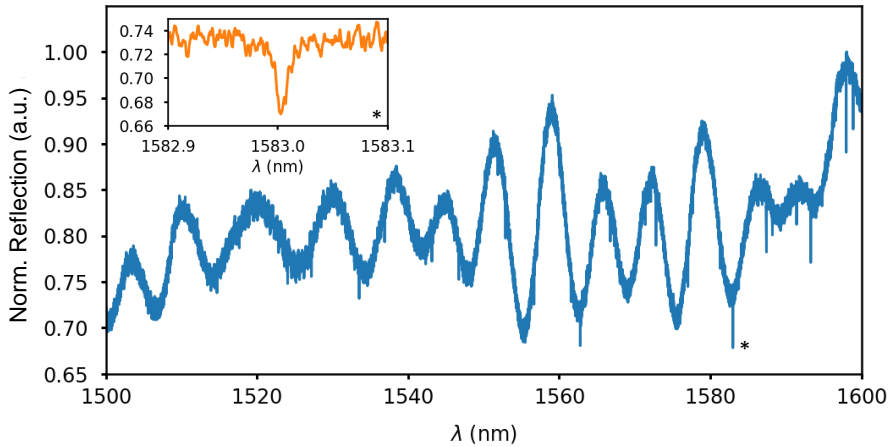


Fig. 5.5: Example PSD spectrum (blue line) of an AVG device displaying evidence of coupling to the whispering gallery mode of the device by the presence of Lorentzian shaped resonances. An optical resonance at ~ 1583 nm is displayed (orange), with an approximate $\Delta\lambda_{\text{FWHM}} = 15$ pm, with an approximate loaded optical Q of 1×10^5 . Most resonances for this particular device display Q 's of $10^4 - 10^5$, with a $\Delta\lambda_{\text{FWHM}}$ being on the order of $\sim 10 - 20$ pm. Evidence of whispering gallery modes is apparent in periodic resonances with $\Delta\lambda_{\text{FSR}} \sim 8$ nm, centred around ~ 1550 nm. The FSR of these resonances are as expected, not constant, becoming more sparse with increasing wavelength. This, in conjunction with the presence of higher order WGM modes, results in resonance ‘doublets’ that visually appear to be aperiodic.

5.3.2 Fabrication issues and design iterating

Fabricating these particularly small devices was not a process free of a handful of challenges. Several iterations had to be fabricated to be able to efficiently couple to the on-chip waveguide, and to correctly release the devices from the silica layer whilst forming a suitable pedestal. Initial attempts saw de-lamination (see Fig. 5.6) of the silicon layer, poor coupling efficiency, and improper device releasing. Firstly, the issue of poor coupling efficiency was solved through lengthening the designed waveguide taper from $15 \mu\text{m}$ to $25 \mu\text{m}$ and adjusting design layouts to minimise optical loss pathways [66]. Secondly, several attempts were taken to successfully release the devices, achieving ‘clean’ and uniform etching of the silica layer. However, the total etch time was over estimated, leading to consistently ‘collapsed’ devices. These collapses can be seen in Fig. 5.6, where it is clear the devices have ‘fallen’ below the height of the top silicon layer. This etching process involves positioning the devices inverted above a bath of HF acid bath (i.e. facing down). This fact, at first glance, makes the suggestion that devices have ‘fallen’ upwards seem unlikely. However, as the pedestals' radii approach zero, van der Waals interaction with the water adsorbed layer causes the devices to stick to the vanishing pedestal. Continued etching of the silica lowers the relative height of the device from the top surface, leading to the van der Waals interaction between the device and the bottom silicon layer being much larger than gravity — indefinitely fixing the devices in place. This would explain the relatively centred but lowered devices displayed in Fig. 5.6.

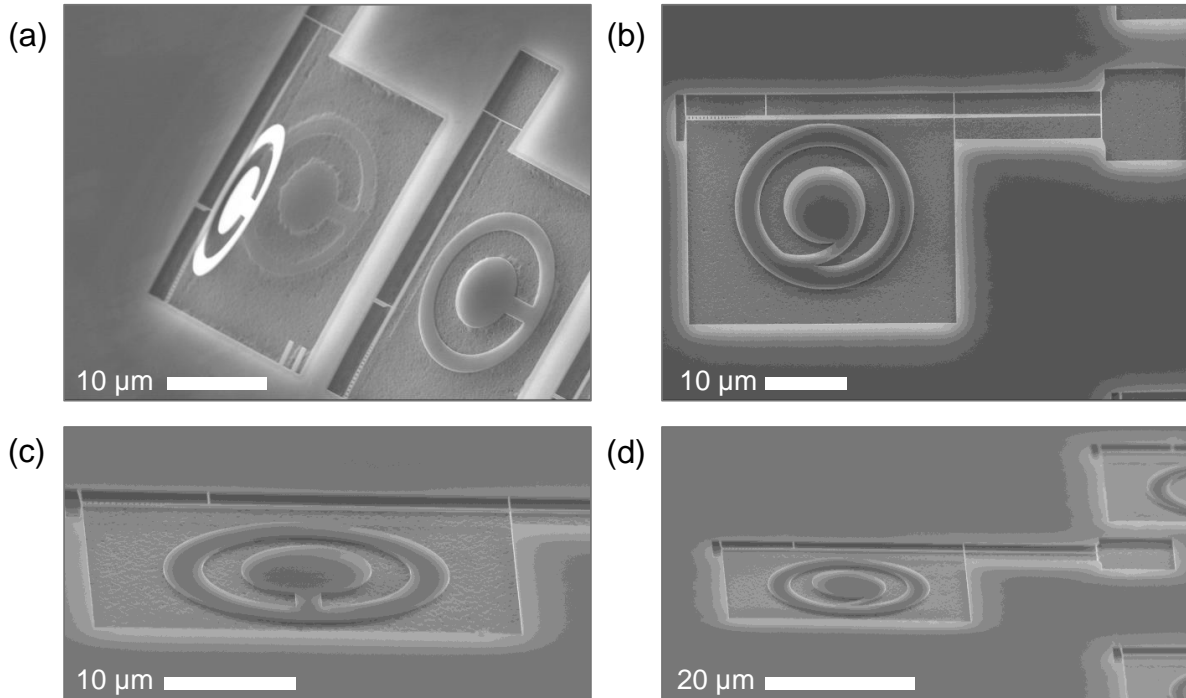


Fig. 5.6: SEM images of early design iterations of AVG devices. (a) De-lamination of top silicon layer from oxide (silica) layer. (b) Top-down view of overall photonic device layout, as per Fig. 5.2. (c) and (d) Collapsed devices due to over etching silica layer and van der Waals ‘stiction’.

The poor coupling efficiency to the coupling waveguide and to the WGM encouraged redesigning of the coupling waveguide tethers. Within the iterations of device design, it was hypothesised that internal stresses from manufacturing processes were released upon etching of the silica layer. This would potentially cause the coupling waveguide to buckle through several mechanisms depending on the nature of the internal stresses, and possibly even cause the disk geometry (annulus) to warp. This buckling would cause misalignment at the coupling site leading to ineffective device coupling, and potentially induce scattering mechanisms from the surrounding chip environment large enough to prevent optical coupling altogether. Prevention of buckling in the central device is not largely achievable without drastically affecting the optical quality of the device, or changing the geometry of the device altogether. Therefore, without direct evidence of this occurring, focus was put on optimising the tethering of the WG to the bulk of the Si chip.

Depending on directions and gradients of internal stresses, buckling may occur several different ways. Briefly, the different kinds of stresses may lead to longitudinal extension or contraction of the WG (along the total length, or localised) and/or tethers. This sort of behaviour can lead to a ‘bowing’ of these narrow components (like squeezing the ends of a flexible rod), deflecting the WG out of plane. In the case of stress gradients in the z -direction, wave-like buckling could also occur. These cases were addressed under several different modifications — making use of ideas around ‘compliant mechanisms’ — varying the thickness, attachment angle, and shape.

5.3.3 Successful fabrication

After implementing many of these design iterations and adjustments to etch times and rates discussed in the previous section, a set of devices were successfully fabricated with minimal issues. However, as outlined previously, chip fabrication involves a set of twin chips, one for imaging. It is important to note that the successful fabrication of devices was isolated to only one of these chips — the other chip experiencing issues during the etching process. The successfully fabricated chip has been used to take the experimental data discussed below, whilst additional fabrication steps were made to recover the second chip for SEM images. The nature of the resonances (to be discussed) strongly suggest that the measured chip consistently displays devices correctly positioned atop of pedestals. As such, the relevant SEM images of AVG devices in this section are not indicative of the results discussed, with devices that are collapsed similar to the iterations discussed in the previous section.

Initial tests of coupling site separations over the range 150 - 450 nm narrowed down optimal distances in the range of 150 - 250 nm. The WGM-WG separation distances of 150 nm, 200 nm, and 250 nm were fabricated for each of the chosen geometries. With several of each design at each separation on a single chip, a (normalised) reflection spectra measured for each to determine which coupling distance is most optimal of the set. Additionally, further investigation of these data sets enables discussion of the viability for a given devices in moving forward in optomechanical superfluid measurements. Typical examples of these data sets are displayed in Fig. 5.7. The control devices (d1) were investigated to determine the most effective coupling distance, i.e. which distance best approaches the critical coupling distance for which $|\mathcal{R}|^2 = 0$. The lack of asymmetry in this device provoked the naïve assumption it is likely the ‘least’ internally flawed across the set of designs. This being the case suggests it is a good benchmark to investigate coupling distance consistently.

The critical coupling distance is unique for a given device, where it is largely dependent on the amount of evanescent field extending out of the coupling waveguide and disk resonator. The refractive index of room temperature bulk Si at 1550 nm is $n_{\text{Si}} = 3.47$ [50]. In waveguides and optical cavities, the evanescent field propagates mostly through vacuum, with refractive index of $n = 1$. In these micro- and even nano-scale devices, a large proportion of the guided light extends outside the cavity, which results in the group velocity of the light to travel at some velocity v_g , with refractive index n_g [50, 62, 64, 67, 68]. Moreover, the implementation of evanescent coupling methods at these small scales is often unique for a given set of dimensions [65]. In this case the silicon coupling waveguide and device have a total thickness of 220 nm, with the waveguide being about 560 nm in width. In combination with the smaller device radius, these dimensions lead to significant enough of a change in the overlap of evanescent fields that the critical coupling distance was smaller than predicted from the past work motivated the initially investigated distances.

Comparing the coupling distances in Fig. 5.7 reveals that optical resonances display relatively high loaded quality factors of $Q \sim 10^5$, with the contrast of the resonances increases with decreasing coupling distance. These high contrast resonances suggest 150 nm is the closest distance to displaying ‘critical coupling’ and will be the distance of interest continuing from here. However, even the largest contrasts are not particularly close to 1, i.e. $|\mathcal{R}|^2 = 1$ just outside the resonance and $|\mathcal{R}|^2 = 0$ inside. This is further complicated by the oscillating

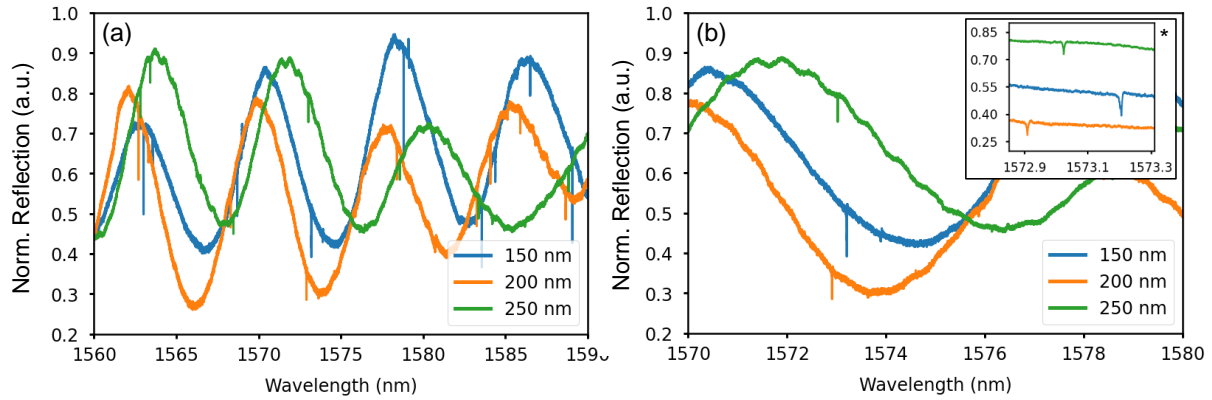


Fig. 5.7: (a) Measured reflected light out of optically coupled d1 device(s) (control) against input laser wavelength. Sinusoidal trend is a result of self-interference of the laser near the coupling site, with sharp drops in measured reflected light being indicative of evanescent coupling of resonant wavelengths to the WGM. (b) Slight shifts in the position of resonant modes can be attributed to minor imperfections or defects from the fabrication process, and from the polarisation dependence of allowed modes in the cavity. The polarisation of the input laser was kept fixed for each acquisition, however the change in spatial separation and/or position of the tapered coupling fibre may have affected the polarisation in the WG. (b)* The (loaded) optical quality factor Q of each of the separations were on the order of $\sim 10^5$ ($\lambda_0 \sim 1573$ nm and $\Delta\lambda_{FWHM} \sim 4$ pm). However, the ‘contrast’ of each resonance clearly increases with decreasing separation. Though this is evidence the system approaches critical coupling, it also enables depositing more optical power into the cavity, a property useful in driving superfluid helium on the AVGs.

spectra, but is still indicative that the critical coupling distance is less than 150 nm.

The reflection spectra of designs d1 and d2 display very large loaded optical Q 's, surpassing 10^5 , and very respectable contrast ratios. The annuli of these designs are well supported by the injecting arm that connects them to their respective central disks, despite the fact that they are relatively thin at first glance. This is a consequence of the exceptionally small device sizes, where the volume decreases by the distance cubed, and the surface area decreases by the distance squared. This enables minimal ‘tilting’ of the device designs d1 and d2 despite their small connecting arms. However, d3's substantially narrower and tapered arm is not rigid enough to support the device. This leads to tilting that moves the edge of the annulus out side of a reasonable coupling distance to the waveguide, resulting in the lack of optical resonances in Fig. 5.8 (a). Further evidence of this being the case is displayed in Fig. 5.9, where SEM imaging of d3 designs suggests that the AVG is in fact misaligned, and intentional mechanical deflection of the coupling waveguide gives rise to small but discernible coupling to the WGM. This suggests that investigation of the effects of tapered or thinner injection arms requires modifications to prevent this tilting. This may involve rotating the position of the arm 90 degrees, aligning the axis of tilt perpendicular to the coupling site to minimise misalignment. More robust solutions may involve modifying the geometry by increasing the number of injection arms — though this would require additional investigation on locked circulation. Consider an additional injection arm, creating a geometry of genus 2 (a two-holed torus), where two topological defects are available for circulation to pin too.

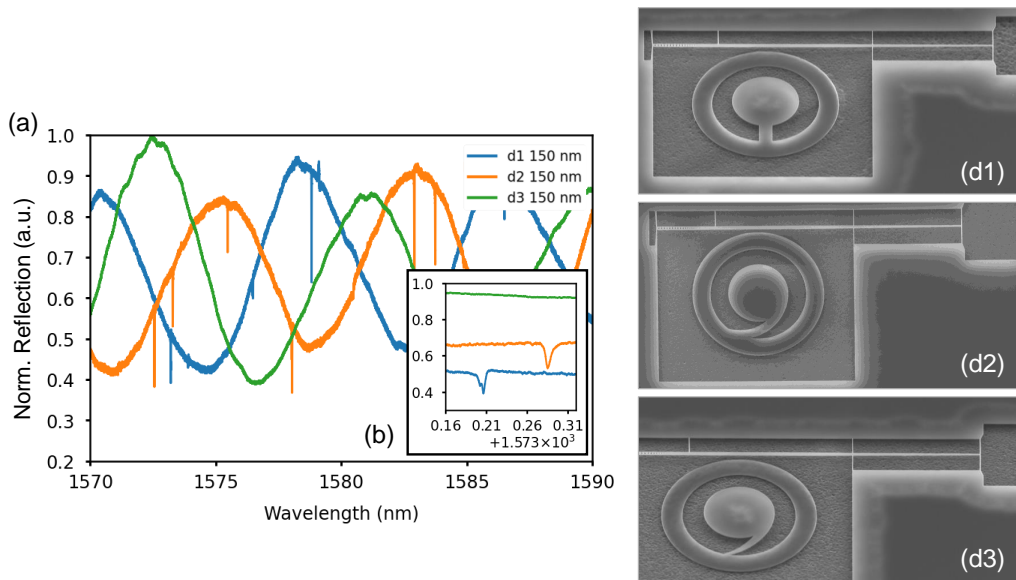


Fig. 5.8: (a) Reflection spectra for each of investigate device design: d1 and d2 show high contrast resonances at 150 nm WGM-WG separation distance, indicating efficient evanescent coupling to the mode. However, the reflection spectra of many different d3 devices display very little evidence of successful coupling to the resonator across all separations, indicating a design specific flaw. (b) Comparing resonant wavelengths in a similar range to Fig. 5.7, the Q value for d1 and d2 here are on the same order of magnitude of $\sim 10^5$. Each device display $\Delta\lambda_{FSR}$ of approximately 8 nm around $\lambda = 1550$ nm, consistent with initial investigations in Fig.5.5.

Despite this being an interesting possibility, the added complexity is outside the scope of this work.

Optical modes in high quality optical devices can be very sensitive to small imperfections in the path of the confined light. This can result in ‘normal mode splitting’, where an imperfection can split a resonant mode into two. This is closely related to the mode splitting sensing modality discussed in Fig. 3.2, and acoustic mode splitting. Picturing a confined standing mode in a WGM resonator as super position of two counter-propagating modes, the splitting arises when the imperfection disturbs a node or anti-node, slightly changing the path length of the resonator. This sort of splitting is seen in the resonance at ~ 1573.2 nm for d1 in Fig. 5.8. These effects are important to consider when choosing a resonant frequency to drive an optical cavity.

The characterisation of these devices, particularly their resonances, is essential in moving towards superfluid control for future experimentation. This often necessitates precise knowledge of the location and shape of resonances and respective optical Q ’s. A Lorentzian (see Eq. 3.21) can be fitted to these resonances to build a more precise and quantitative description of relevant parameters. However, this should be done under the right conditions to best describe the resonator when experimenting with superfluid helium. The thermo-optic coefficient of silicon is positive ($\frac{dn}{dT} = 1.87 \times 10^{-4} \text{ K}^{-1}$ at 1500 nm), meaning the vastly

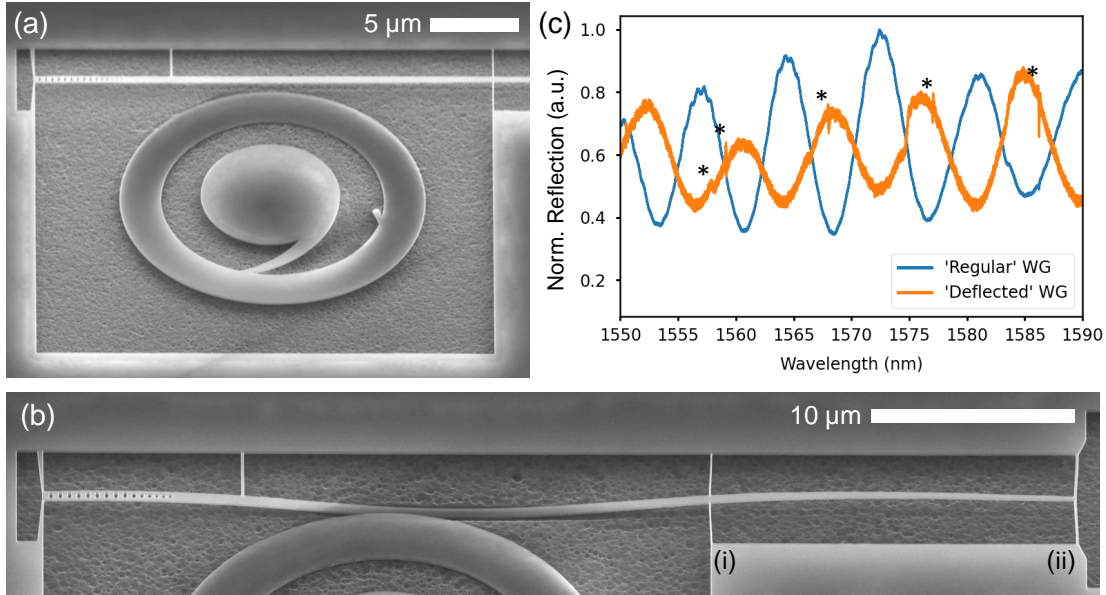


Fig. 5.9: (a) SEM image of device design d3(d). The shadow under the near edge of the device and the lack of a similar shadow on the far edge suggests possible ‘tilting’ of the annulus, and hence misalignment of the WGM with the coupling WG from out-of-plane strain. (b) Buckling of coupling waveguide is sustained by van der Waals interactions with the substrate. The large aspect ratio of the integrated photonic WG can lead to substantial deflection with even minute forces. Typically, optical coupling involves positioning a tapered fibre along the tapered end of the coupling WG of a device, with the tip of the fibre positioned at tether (i) pointed towards the mirror — a structurally well supported region. (c) Coupling to this device in this way consistently yields little evidence of evanescent coupling to the WGM. However, positioning the tip of the optical fibre past tether (i) — away from (ii) — can ‘deflect’ the WG downwards, which often yields poor, but evident, coupling to the WGM (see *).

colder temperatures required for superfluidity than room temperatures leads to a change in the refractive index, and hence resonance condition of the resonators [50]. Moreover, the application of a superfluid helium thin film, even in equilibrium, will disturb the medium the evanescent field propagates through leading to a measurable effect on the resonant frequency. This effect is the predominate mechanism in measuring superfluid helium film thicknesses in practice [35]. Quantitative knowledge of the resonant wavelengths, optical Q 's and other parameters can prove useful in determining the viability of a given design for future experiment, and in optimising future designs. A numerical data fitting to a Lorentzian (converting ω to λ in Eq. 3.21) at the resonant wavelength of ~ 1578.8 nm for d1 at 150 nm is displayed in Fig. 5.10.

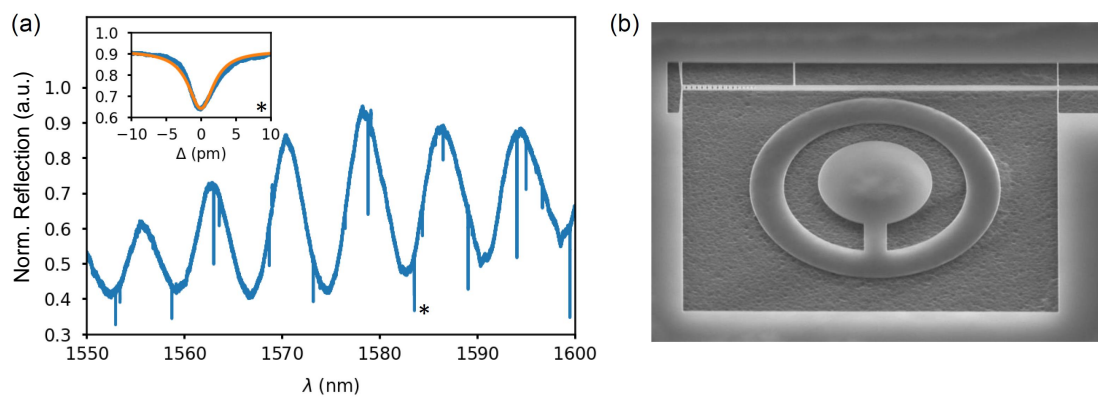


Fig. 5.10: (a) Example data fitting to a Lorentzian (orange) of the form in Eq. 3.21 for a reflection spectrum (blue) of device d1 (b) (150 nm coupling distance) and resonance wavelength of $\lambda_0 = 1578.814$ nm.

6

Surface tension and superfluid helium thin-films

The ability to calculate surface profiles of vortices under the influence of surface tension allows for better investigation of how light reflects and refracts in these thin-films, valuable information in moving towards real-time and non-destructive vortex imaging for superfluid helium thin-films. This sort of vortex detection scheme has yet to be achieved in superfluid helium thin-film experiments, where the small refractive index of the helium ($n = 1.029$) and small fluid volumes result in only weak interactions with probing or imaging lights.

Developing an imaging scheme to achieve this is a long term goal within the lab. In collaboration with PhD student D. Harvey, surface tension effects of many vortices in thin-film superfluid helium has been investigated — a topic not well discussed in literature. The following chapter will outline implemented computational methods in this investigation, and the implications of numerical results for single vortex imaging.

6.1 Real-time vortex microscopy for superfluid ^4He

Interferometric scattering microscopy (iSCAT) techniques are used for many applications of small particle detection in solutions, particularly in biological applications [69, 70]. Understanding the effects of a vortex with optical probes (i.e. light rays) is critical in applying this proposed technique for superfluid helium ‘vortex microscopy’. The ability to calculate the physical surface profile of interacting vortices is incredibly useful here. However, knowledge of *where* a vortex may be is just as important for experiment. In order to study the dynamics of several vortices for an extended period of time would enable investigation of many phenomena that are not well understood.

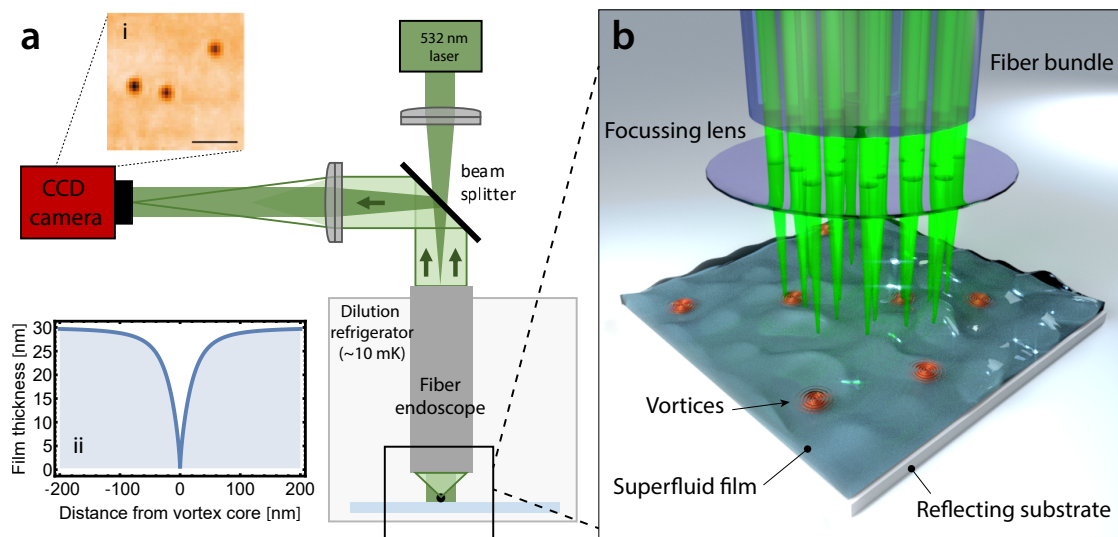


Fig. 6.1: Proposed vortex microscopy detection scheme for real-time, non-destructive imaging. (a) General experimental implementation of interferometric scattering microscopy (iSCAT) for superfluid helium vortex detection, enabled by the (weak) interaction of light with vortex ‘dimples’. (b) Rendered diagram of superfluid helium thin-film with microscope objective. Credit: Dr. C. G. Baker.

6.2 Surface tension in superfluid helium thin-films

The total chemical potential μ of a fluid can be described as the sum of each contribution of energy. A common set of energy contributions is the kinetic energy, van der Waals interaction (with a substrate), and gravity, respectively giving

$$\mu = \mu_{\text{KE}} + \mu_{\text{vdW}} + \mu_g \quad (6.1)$$

$$\mu \approx \frac{1}{2} v_s(\vec{r})^2 - \frac{\alpha_{\text{vdW}}}{d^3}, \quad (6.2)$$

with the approximation that $\mu_g \ll \mu_{\text{vdW}}$, where μ_{KE} is the specific kinetic energy due to flow around a vortex core, and surface waves are ignored. In equilibrium, the surface of a film obeys this equivalence. This expression is a general statement, but we will take the van der Waals interaction coefficient α_{vdW} as that between silicon and helium-4, with $\alpha_{\text{vdW}} = 3.5 \times 10^{-24} \text{ m}^5 \text{s}^{-2}$ [71]. The assumption that the van der Waals interaction strength dominates over gravity is well justified in the limit of very thin films. Recent works in superfluid helium thin-films have shown that thicknesses of less than 30 nm are comfortably achievable, with strongly justified quasi-2D assumptions for several nanometre thicknesses and sufficiently low temperatures ($\sim 10 \mu\text{K}$) [8, 72]. For consistency, film-thicknesses discussed in this chapter will be taken as $d_0 = 30 \text{ nm}$, assuming no vertically propagating energy modes, consistent with our definition of a 2D superfluid. The van der Waals interaction acts as an effective gravity for the superfluid. For a silicon substrate and film thickness of 30 nm, this effective gravity is $g_{\text{vdW}} = 3\alpha_{\text{vdW}}/d^4 \simeq 10^7 \text{ m s}^{-2}$, whilst on the surface of Earth, the acceleration due to gravity is famously $g \simeq 10 \text{ m s}^{-2}$, six orders of magnitude smaller. If $\mu = \mu_0$ is taken to be the constant $-\alpha_{\text{vdW}}/d_0^3$, with d_0 being the film thickness far away from a vortex, Eq. 6.2

can be rewritten as an expression for the film depth as

$$d = \left(\frac{\alpha_{\text{vdW}}}{\frac{\alpha_{\text{vdW}}}{d_0^3} + \frac{1}{2} v_s(\vec{r})^2} \right)^{1/3}. \quad (6.3)$$

What remains is an analytically solvable expression for the surface height of a thin-film, given the velocity field is known. With the help of potential flow theory, the velocity field of vortices can be ‘imprinted’, and the resultant film shape can be calculated. The essence of potential flow theory is describing the velocity by the form $\vec{v}_s(x, y) = \nabla\Phi$, where Φ is called the velocity potential. Without derivation, the stream-function of a single vortex at $(X_1, 0)$ with charge κ on a 2D plane is

$$\Phi = \pm \frac{\kappa}{2\pi} \left(\ln \sqrt{(x - X_1)^2 + y^2} \right), \quad (6.4)$$

where the \pm refers to the relative ‘sign’ or direction of circulation around the core [73]. The stream function then provides the velocity components as

$$v_{sx} = \frac{\partial\Phi}{\partial y} \quad \text{and} \quad v_{sy} = -\frac{\partial\Phi}{\partial x}. \quad (6.5)$$

These expressions can be used with Eq. 6.3 to determine the surface profile of a superfluid film due to a point vortex (or vortices). An important consideration is the critical velocity of the superfluid, for which the kinetic energy surpasses the superfluid transition energy ε_c . At radial distances close to the vortex core the fluid fraction becomes predominately of normal fluid — where the critical velocity here has been taken as $v_c = 60$ m/s. This provides a limit on the maximum kinetic energy inside a vortex core, which results in a core ‘height’ that does not span the entirety of d_0 . Note here that the velocity contribution of a vortex is a function only of radial distance \vec{r} , with no z dependence. However, the surface tension of superfluid ${}^4\text{He}$ is not negligible in these regimes. By enforcing the pressure at the surface to be balanced with the fluid above (or lack thereof), surface tension imparts a chemical potential energy contribution of $\mu_\sigma = \Delta P_\sigma / \rho_s$, where ρ_s is the superfluid density. The pressure term ΔP_σ comes from the Young-Laplace equation and is of the form

$$\Delta P_\sigma = 2\sigma H, \quad (6.6)$$

where σ is the surface tension, and H is the mean curvature of the surface. For a general geometry, the mean curvature is

$$H = \frac{1}{2} \left(\frac{1}{R_x} + \frac{1}{R_y} \right), \quad (6.7)$$

where R_x and R_y are the radii of curvature in the respective directions of the surface, which themselves are given by

$$R_x = \frac{\left(1 + \left(\frac{\partial z}{\partial x}\right)^2\right)^{3/2}}{\frac{\partial^2 z}{\partial x^2}} \quad \text{and} \quad R_y = \frac{\left(1 + \left(\frac{\partial z}{\partial y}\right)^2\right)^{3/2}}{\frac{\partial^2 z}{\partial y^2}}. \quad (6.8)$$

The introduction of surface tension into Eq. 6.2 results in a differential equation for the film thickness at any point by the need of calculating the mean curvature H of the surface. More broadly speaking, this energy contribution for a given point is dependent on its neighbouring points. Again ignoring the small contribution from gravity, the chemical potential of the surface of the film must now obey

$$\mu_0 = \mu_{\text{KE}} + \mu_{\text{vdW}} + \mu_\sigma \quad (6.9)$$

$$-\frac{\alpha_{\text{vdW}}}{d_0^3} = \frac{1}{2} v_s(\vec{r})^2 - \frac{\alpha_{\text{vdW}}}{d^3} + \sigma \left(\frac{1}{R_x} + \frac{1}{R_y} \right). \quad (6.10)$$

This can be solved exactly using a Green's function for a radially symmetric surface profile [10]. So then, the surface profile of *one* vortex is exactly solvable, but not *multiple* vortices. For n vortices, computationally expensive numerical solutions are necessary. For superfluid helium, a majority of this computational cost comes simply from the large spatial domain sizes of microns for which a vortex will distort a surface, whilst still needing a fine enough spatial discretisation to capture the angstrom sized vortex cores of large mean curvature. Approaching this with a brute force method would require hundreds of thousands of grid points for even calculating the surface profile of a single pair of vortices. However, understanding the shape and displaced volume of a vortex on these surfaces is critical in progressing towards detection of vortices at single vortex resolutions — a feat yet to be achieved in practice. Moving towards this goal of direct imaging prompts the improvement of understanding the effects of surface tension on superfluid helium vortices. An optimised numerical method for solving Eq. 6.10 is the first step in this process.

6.3 Vortices in ${}^4\text{He}$ thin-films with surface tension

As mentioned, a majority of computational expense stems from the need for many grid points. A robust solution to this is the use of non-constantly spaced grid points. Implementing this sort of discretisation scheme enables localised dense ‘meshing’ of grid points near a vortex core, and more sparsely spaced points far away where the mean curvature is ‘smaller’. Distributing grid points from the origin of a vortex core, the distance between a point and the subsequent can be governed by a function of the form

$$\Delta x_i \propto x^{-1/p}, \quad (6.11)$$

where p is some real number larger than 1. This distributes more grid points for distances near a vortex core. The general problem of solving Eq. 6.10 can be done using an iterative approach. Here an ‘error’ is attributed between the chemical potential μ_0 and the chemical potential of any given point on the surface of the film when calculated according to Eq. 6.10. The sign and magnitude of this error can be used to ‘anneal’ the height of the surface at every point, where positive errors lead to an increase in film height, and negative errors a decrease — see Fig. 6.2 (a). Over many iterations, this error reduces as the film approaches a stable solution for which the total chemical potential is uniform. Implementing this method for a single vortex can be done, and the comparison the film height from the core of a vortex with the analytical Green’s function can be seen in Fig. 6.2 (b) [10]. This iterative scheme

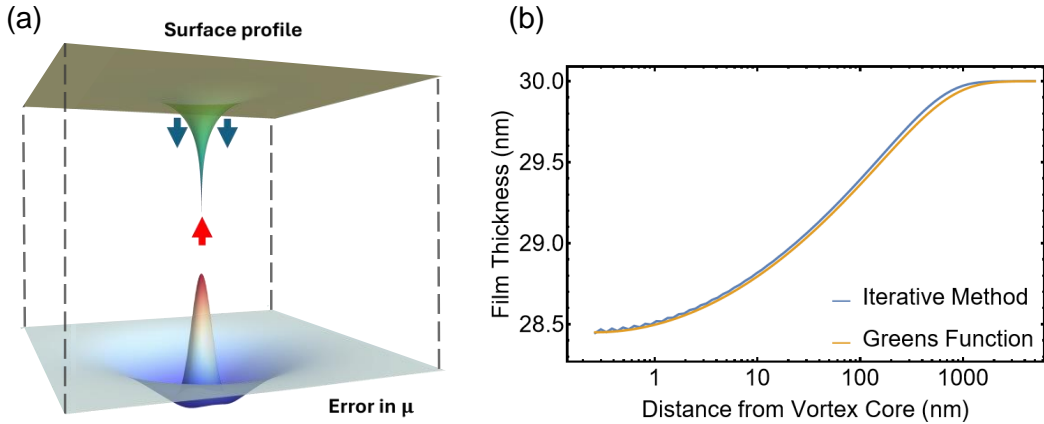


Fig. 6.2: Iterative numerical approach in solving the surface profile of a vortex in a superfluid helium thin-film with surface tension. Locally adjusting the film height dependent on the chemical potential error (a) ‘anneals’ the surface of the film, and well approximates the exact solution for a single vortex (b) for small enough chemical potential error ($\sim 1\%$), enabling the investigation of surface tension for many vortices [10].

in combination of non-linear spatial discretisation provides numerical solutions of a single vortex within 1% error of the exact solution with a modest compute without the need of specialised computing resources.

6.4 Superfluid helium thin-film energies and displaced volumes of vortices

The investigation of n vortices is now reasonably accessible in terms of computational expense. This immediately suggests solving for a vortex pair, and comparing the surface shape to that of a vortex pair without accounting for surface tension. Examples of opposite sign vortex pairs of two separation distances can be found in Fig. 6.3, though same sign pairs are no less calculable. The inclusion of surface tension for these thin-film vortices results in ‘penetration’ depth of the vortex into the surface of the film dramatically decreasing compared to the case of no surface tension. Despite this, the film height further from the core is lowered, and as a result, the total displaced volume of the vortices are left mostly unchanged, calculated with

$$V_{\text{disp}} = V_0 - \iint z \, dx \, dy, \quad (6.12)$$

where V_0 is the volume of the vortex free film of thickness d_0 . At first glance, this is unclear from Fig. 6.3 (a), though the distance for which the surface is lowered is significant, and the resulting radial volume element becomes very large. Though this is the case, the *distribution* of displaced volume is of course changed dramatically. This has many implications for vortex detection schemes for superfluid helium. For instance, in the case of superfluid optomechanics

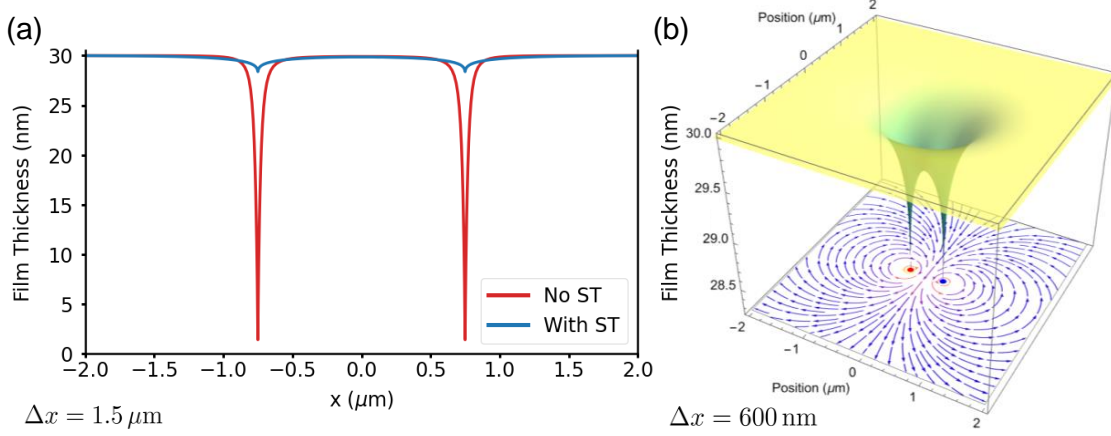


Fig. 6.3: Iteratively solved solutions of vortex-antivortex pairs in a superfluid helium thin-film with the inclusion of surface tension separated by a distance Δx , see Eq. 6.3. (a) A cross-section of the 3D surface reveals a drastic change in the shape of the ‘dimple’ a vortex leaves on the surface when compared to a surface tension-free solution. (b) 3D surface plot of vortex-antivortex pair and the corresponding velocity streamlines of the quantum vortices.

the larger size of the vortex with unchanged total displaced volume will impact the resultant resonant frequency shift for when a vortex disturbs the optical field of a cavity.

6.5 Single vortex traps for superfluid ^4He

Different optomechanical resonator substrates may have different strengths of van der Waals interaction with superfluid helium, and in particular, gold interacts more strongly than the silicon substrates we have looked at so far. Fabrication techniques enable the ability to deposit thin layers of gold on a silicon or silica substrate [74]. Doing this provides regions of increased superfluid height for thin-films. An example of this is shown in Fig. 6.4, where a ring of gold forms a smooth static fluid ‘well’ from the influence of surface tension. These wells are proposed to be a method for trapping vortices, enabling better application of the previously proposed iSCAT vortex imaging techniques.

The inclusion of surface tension, as discussed, changes the distribution of displaced volume in a film, and hence changes the energy of the particles in the film. Understanding how the total energy of a ‘gold ring’ film changes for varying positions of a vortex allows us to determine the viability of these traps. The kinetic energy of the film is given by

$$E_{\text{KE}} = \iint \frac{1}{2} \rho_s v_s(x, y)^2 dx dy, \quad (6.13)$$

where ρ_s is the density of the superfluid, which we will take as superfluid helium, with $\rho_s = 145 \text{ kg m}^{-3}$ [10, 75]. The surface tension energy E_{ST} contributed by the additional

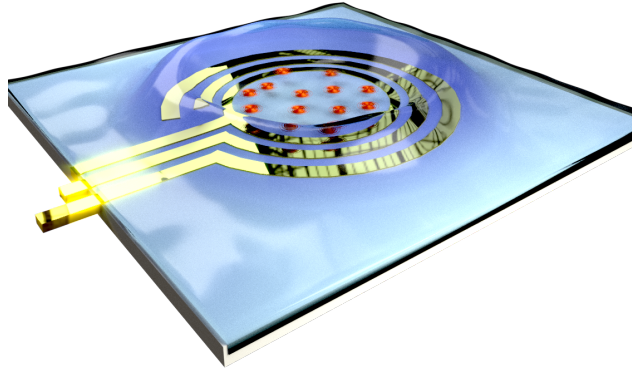


Fig. 6.4: Rendition of gold deposited on a silica substrate demonstrating proposed vortex trapping through the ‘fluid well’ cause by the stronger interaction of superfluid helium with gold than silica. Several gold rings are depicted, where the proposal to apply a voltage across these electrodes is made to electrically tune the height of the trap. Credit: Dr. C. G. Baker.

surface are of a vortex dimple is

$$E_{\text{ST}} = \sigma \iint \sqrt{1 + (\partial_x z)^2 + (\partial_y z)^2} - 1 \, dx \, dy, \quad (6.14)$$

where $\sigma = 3.5 \times 10^{-4} \text{ J m}^{-2}$ is the surface tension for superfluid helium-4 [10, 75]. The region of deformed film surface in the presence of a vortex gives rise to variations of the strength of the van der Waals interaction in the z direction. This results in a potential energy associated with missing fluid being ‘moved’ elsewhere (i.e. into a reservoir of height d_0), and can be calculated with

$$E_{\text{pot}} = \rho_s \iint \left(\frac{\alpha_{\text{vdw}}}{2(d_0 + \eta(x, y))^2} - \frac{\alpha_{\text{vdw}}}{2d_0^2} \right) \, dx \, dy - \rho_s V_{\text{disp}} \frac{-\alpha_{\text{vdW}}}{d_0^3}, \quad (6.15)$$

where $\eta(x, y)$ is the ‘surface amplitude oscillation’, similar to the amplitude of a wave from the mean fluid height [35]. This final term enables the calculation of the total energy of a film (at constant volume) with

$$E = E_{\text{ST}} + E_{\text{KE}} + E_{\text{pot}}. \quad (6.16)$$

From here, a static surface profile that includes a ‘gold ring’ in the substrate can be constructed, and the total energy E in the presence of a vortex can be calculated as the vortex ‘moves’ from the centre to far away. Fig. 6.5 displays such an investigation, where the centre of the trap is not a global minimum, but is in fact a local minimum.

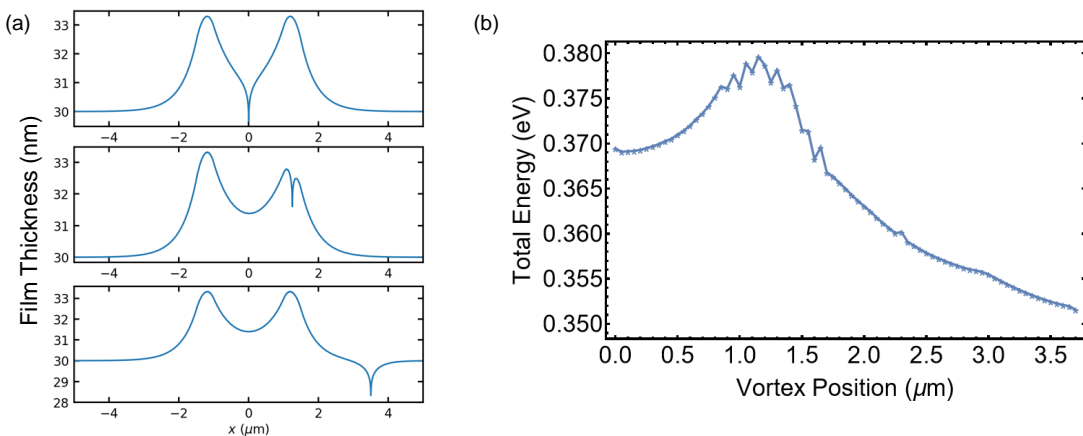


Fig. 6.5: **a** Cross-sections of a vortex positions in, on, and far away from a superfluid well induced by locally increased van der Waals interactions of the substrate (see Fig. 6.4). **(b)** The calculated total energy of the film for increasing radial position of the vortex from the centre of the well, according to Eq. 6.16.

The total energy minima within the centre of the gold ring trap suggests the possibility of isolating one or several vortices. The ability to do this in tandem with real time imaging would provide a platform in observing superfluid vortex dynamics in an unprecedented manner, enabling investigation of many ill-understood quantum vortex phenomena. Though what is yet to be discussed is how vortices might be placed in the trap. Brute force approaches like directing many vortices may work well, though it is likely the interaction of a trapped vortex with any nearby vortices would provide it enough kinetic energy to escape the trap. However, a more controllable approach may be possible, where applying a voltage across the gold ring can cause attraction of superfluid helium through induced dipole moment interactions, as mentioned in Fig. 6.4. This motivates a ‘tunable’ vortex trap, with the ability to adjust the height of the trap, above that of just the static van der Waals attraction discussed above. With this, it is feasible to overcome the challenges associated with directing vortices into the trap simply by injecting several vortices into a ‘flat’ surface, only to swiftly switch on the fluid well in hopes of trapping several vortices. Additionally, engineered vortex generation within the trap, where background velocities above v_c past an obstacle may nucleate vortices, transferring the fluids linear momentum into angular momentum, leaving the vortices with insufficient kinetic energy to escape the trap.

7

Outlook and Conclusion

This thesis has covered the investigation of engineered directional flow and controlled vortex generation using integrated superfluid circuits, progressing towards the observation of single quanta of circulation in two-dimensional superfluid helium thin-films. This investigation started with computational modelling of superfluid dynamics in whispering gallery mode resonators, namely in the novel geometry of an angular vortex generator. Potential flow theory was employed to understand the steady state flow attributed to laser-induced evaporation of superfluid helium coated AVG photonic devices. This understanding was used to apply a ‘driven’ dGPE to simulate the superfluid dynamics of a modelled experimental implementation of AVGs. Through investigation of the effects of various design parameters, these dGPE simulations were used in optimisation of potentially viable AVG designs for experimental implementation. Promising designs from this process were integrated into an on-chip silicon photonic device design. The successful fabrication and characterisation of angular vortex generators puts this work tantalisingly close to observing superfluid dynamics in AVGs. This has extreme promise in the first observation of single quanta of circulation in superfluid helium thin-films in the 2D realm for the first time. Additionally covered is the investigation of the effects of surface tension on superfluid helium thin-films in the presence of an arbitrary number of vortices. This focused on optimising the computational methods involved in numerically calculating the surface of a fluid film. These results are important in moving towards real-time, non-destructive single vortex imaging, and in the development of single vortex traps.

References

- [1] L. Xu, X. Jiang, G. Zhao, D. Ma, H. Tao, Z. Liu, F. G. Omenetto, and L. Yang. *High-Q silk fibroin whispering gallery microresonator*. Optics Express **24**(18), 20825 (2016). Publisher: Optica Publishing Group, URL <https://opg.optica.org/oe/abstract.cfm?uri=oe-24-18-20825>.
- [2] J. Zhu, S. K. Ozdemir, Y.-F. Xiao, L. Li, L. He, D.-R. Chen, and L. Yang. *On-chip single nanoparticle detection and sizing by mode splitting in an ultrahigh-Q microresonator*. Nature Photonics **4**(1), 46 (2010). URL <https://www.nature.com/articles/nphoton.2009.237>.
- [3] L. Shao, X.-F. Jiang, X.-C. Yu, B.-B. Li, W. R. Clements, F. Vollmer, W. Wang, Y.-F. Xiao, and Q. Gong. *Detection of Single Nanoparticles and Lentiviruses Using Microcavity Resonance Broadening*. Advanced Materials **25**(39), 5616 (2013). URL <https://onlinelibrary.wiley.com/doi/abs/10.1002/adma201302572>.
- [4] X. Jiang, A. J. Qavi, S. H. Huang, and L. Yang. *Whispering-Gallery Sensors*. Matter **3**(2), 371 (2020). URL <https://linkinghub.elsevier.com/retrieve/pii/S2590238520303660>.
- [5] W. P. Bowen, C. G. Baker, and J. G. E. Harris. *Chapter Six - Superfluid SBS*. In B. J. Eggleton, M. J. Steel, and C. G. Poulton, eds., *Semiconductors and Semimetals*, vol. 109 of *Brillouin Scattering Part 1*, pp. 193–225 (Elsevier, 2022). URL <https://www.sciencedirect.com/science/article/pii/S0080878422000047>.
- [6] Y. L. Sfendla, C. G. Baker, G. I. Harris, L. Tian, R. A. Harrison, and W. P. Bowen. *Extreme quantum nonlinearity in superfluid thin-film surface waves*. npj Quantum Information **7**(1), 1 (2021). Publisher: Nature Publishing Group, URL <https://www.nature.com/articles/s41534-021-00393-3>.
- [7] A. Sawadsky, R. A. Harrison, G. I. Harris, W. W. Wasserman, Y. L. Sfendla, W. P. Bowen, and C. G. Baker. *Engineered entropic forces allow ultrastrong dynamical back-action*. Science Advances **9**(21), eade3591 (2023). Publisher: American Association for the Advancement of Science, URL <https://www.science.org/doi/full/10.1126/sciadv.ade3591>.
- [8] Y. P. Sachkou, C. G. Baker, G. I. Harris, O. R. Stockdale, S. Forstner, M. T. Reeves, X. He, D. L. McAuslan, A. S. Bradley, M. J. Davis, and W. P. Bowen. *Coherent vortex*

- dynamics in a strongly interacting superfluid on a silicon chip.* Science (New York, N.Y.) **366**(6472), 1480 (2019).
- [9] C. Brown, Y. Wang, M. Namazi, G. Harris, M. Uysal, and J. Harris. *Superfluid Helium Drops Levitated in High Vacuum.* Physical Review Letters **130**(21), 216001 (2023). Publisher: American Physical Society, URL <https://link.aps.org/doi/10.1103/PhysRevLett.130.216001>.
 - [10] E. Vittoratos, M. W. Cole, and P. P. M. Meincke. *Free Surface of a Rotating HeII Film.* Canadian Journal of Physics **51**(21), 2283 (1973). URL <http://www.nrcresearchpress.com/doi/10.1139/p73-298>.
 - [11] J. F. Allen and H. Jones. *New Phenomena Connected with Heat Flow in Helium II.* Nature **141**(3562), 243 (1938). Publisher: Nature Publishing Group, URL <https://www.nature.com/articles/141243a0>.
 - [12] P. Kapitza. *Viscosity of Liquid Helium below the λ -Point.* Nature **141**(3558), 74 (1938). Publisher: Nature Publishing Group, URL <https://www.nature.com/articles/141074a0>.
 - [13] C. Enss and S. Hunklinger. *Low-Temperature Physics* (Springer-Verlag, Berlin/Heidelberg, 2005). URL <http://link.springer.com/10.1007/b137878>.
 - [14] S. Balibar. *Laszlo Tisza and the two-fluid model of superfluidity.* Comptes Rendus. Physique **18**(9-10), 586 (2017). URL <https://comptes-rendus.academie-sciences.fr/physique/articles/10.1016/j.crhy.2017.10.016/>.
 - [15] S. Spence, Z. Koong, S. Horsley, and X. Rojas. *Superfluid Optomechanics With Phononic Nanostructures.* Physical Review Applied **15**(3), 034090 (2021). Publisher: American Physical Society, URL <https://link.aps.org/doi/10.1103/PhysRevApplied.15.034090>.
 - [16] J. R. T. Seddon, M. S. Thurlow, M. J. Lees, and P. G. J. Lucas. *Quantised vortex line visualisation in superfluid helium using low-temperature optics.* Physica B: Condensed Matter **329-333**, 220 (2003). URL <https://www.sciencedirect.com/science/article/pii/S092145260201966X>.
 - [17] M. T. Reeves, T. P. Billam, X. Yu, and A. S. Bradley. *Enstrophy Cascade in Decaying Two-Dimensional Quantum Turbulence.* Physical Review Letters **119**(18), 184502 (2017). Publisher: American Physical Society, URL <https://link.aps.org/doi/10.1103/PhysRevLett.119.184502>.
 - [18] A. Guthrie, S. Kafanov, M. T. Noble, Y. A. Pashkin, G. R. Pickett, V. Tsepelin, A. A. Dorofeev, V. A. Krupenin, and D. E. Presnov. *Nanoscale real-time detection of quantum vortices at millikelvin temperatures.* Nature Communications **12**(1), 2645 (2021). Publisher: Nature Publishing Group, URL <https://www.nature.com/articles/s41467-021-22909-3>.

- [19] E. Varga, V. Vadakkumbatt, A. Shook, P. Kim, and J. Davis. *Observation of Bistable Turbulence in Quasi-Two-Dimensional Superflow*. Physical Review Letters **125**(2), 025301 (2020). Publisher: American Physical Society, URL <https://link.aps.org/doi/10.1103/PhysRevLett.125.025301>.
- [20] S. Forstner, Y. Sachkou, M. Woolley, G. I. Harris, X. He, W. P. Bowen, and C. G. Baker. *Modelling of vorticity, sound and their interaction in two-dimensional superfluids*. New Journal of Physics **21**(5), 053029 (2019). Publisher: IOP Publishing, URL <https://dx.doi.org/10.1088/1367-2630/ab1bb5>.
- [21] X. Rojas and J. P. Davis. *Superfluid nanomechanical resonator for quantum nanofluidics*. Physical Review B **91**(2), 024503 (2015). Publisher: American Physical Society, URL <https://link.aps.org/doi/10.1103/PhysRevB.91.024503>.
- [22] J. M. Kosterlitz and D. J. Thouless. *Ordering, metastability and phase transitions in two-dimensional systems*. Journal of Physics C: Solid State Physics **6**(7), 1181 (1973). URL <https://dx.doi.org/10.1088/0022-3719/6/7/010>.
- [23] D. J. Bishop and J. D. Reppy. *Study of the Superfluid Transition in Two-Dimensional ^4He Films*. Physical Review Letters **40**(26), 1727 (1978). Publisher: American Physical Society, URL <https://link.aps.org/doi/10.1103/PhysRevLett.40.1727>.
- [24] P. Minnhagen. *The two-dimensional Coulomb gas, vortex unbinding, and superfluid-superconducting films*. Reviews of Modern Physics **59**(4), 1001 (1987). URL <https://link.aps.org/doi/10.1103/RevModPhys.59.1001>.
- [25] R. Desbuquois, L. Chomaz, T. Yefsah, J. Léonard, J. Beugnon, C. Weitenberg, and J. Dalibard. *Superfluid behaviour of a two-dimensional Bose gas*. Nature Physics **8**(9), 645 (2012). Publisher: Nature Publishing Group, URL <https://www.nature.com/articles/nphys2378>.
- [26] D. K. Armani, T. J. Kippenberg, S. M. Spillane, and K. J. Vahala. *Ultra-high-Q toroid microcavity on a chip*. Nature **421**(6926), 925 (2003). Publisher: Nature Publishing Group, URL <https://www.nature.com/articles/nature01371>.
- [27] V. R. Almeida and M. Lipson. *Optical bistability on a silicon chip*. Optics Letters **29**(20), 2387 (2004). Publisher: Optica Publishing Group, URL <https://opg.optica.org/ol/abstract.cfm?uri=ol-29-20-2387>.
- [28] T. J. Kippenberg, H. Rokhsari, T. Carmon, A. Scherer, and K. J. Vahala. *Analysis of Radiation-Pressure Induced Mechanical Oscillation of an Optical Microcavity*. Physical Review Letters **95**(3), 033901 (2005). Publisher: American Physical Society, URL <https://link.aps.org/doi/10.1103/PhysRevLett.95.033901>.
- [29] G. Anetsberger, O. Arcizet, Q. P. Unterreithmeier, R. Rivière, A. Schliesser, E. M. Weig, J. P. Kotthaus, and T. J. Kippenberg. *Near-field cavity optomechanics with nanomechanical oscillators*. Nature Physics **5**(12), 909 (2009). Publisher: Nature Publishing Group, URL <https://www.nature.com/articles/nphys1425>.

- [30] J. Ward and O. Benson. *WGM microresonators: sensing, lasing and fundamental optics with microspheres.* Laser & Photonics Reviews **5**(4), 553 (2011). URL <https://onlinelibrary.wiley.com/doi/abs/10.1002/lpor.201000025>.
- [31] M. Aspelmeyer, T. J. Kippenberg, and F. Marquardt. *Cavity optomechanics.* Reviews of Modern Physics **86**(4), 1391 (2014). Publisher: American Physical Society, URL <https://link.aps.org/doi/10.1103/RevModPhys.86.1391>.
- [32] E. Gil-Santos, C. Baker, D. T. Nguyen, W. Hease, C. Gomez, A. Lemaître, S. Ducci, G. Leo, and I. Favero. *High-frequency nano-optomechanical disk resonators in liquids.* Nature Nanotechnology **10**(9), 810 (2015). Publisher: Nature Publishing Group, URL <https://www.nature.com/articles/nnano.2015.160>.
- [33] N. Toropov, G. Cabello, M. P. Serrano, R. R. Gutha, M. Rafti, and F. Vollmer. *Review of biosensing with whispering-gallery mode lasers.* Light: Science & Applications **10**(1), 42 (2021). Publisher: Nature Publishing Group, URL <https://www.nature.com/articles/s41377-021-00471-3>.
- [34] L. A. D. Lorenzo and K. C. Schwab. *Superfluid optomechanics: coupling of a superfluid to a superconducting condensate.* New Journal of Physics **16**(11), 113020 (2014). Publisher: IOP Publishing, URL <https://dx.doi.org/10.1088/1367-2630/16/11/113020>.
- [35] C. G. Baker, G. I. Harris, D. L. McAuslan, Y. Sachkou, X. He, and W. P. Bowen. *Theoretical framework for thin film superfluid optomechanics: towards the quantum regime.* New Journal of Physics **18**(12), 123025 (2016). Publisher: IOP Publishing, URL <https://dx.doi.org/10.1088/1367-2630/aa520d>.
- [36] L. Childress, M. P. Schmidt, A. D. Kashkanova, C. D. Brown, G. I. Harris, A. Aiello, F. Marquardt, and J. G. E. Harris. *Cavity optomechanics in a levitated helium drop.* Physical Review A **96**(6), 063842 (2017). Publisher: American Physical Society, URL <https://link.aps.org/doi/10.1103/PhysRevA.96.063842>.
- [37] A. D. Kashkanova, A. B. Shkarin, C. D. Brown, N. E. Flowers-Jacobs, L. Childress, S. W. Hoch, L. Hohmann, K. Ott, J. Reichel, and J. G. E. Harris. *Optomechanics in superfluid helium coupled to a fiber-based cavity.* Journal of Optics **19**(3), 034001 (2017). Publisher: IOP Publishing, URL <https://dx.doi.org/10.1088/2040-8986/aa551e>.
- [38] W. F. Vinen. *Detection of Single Quanta of Circulation in Rotating Helium II.* Nature **181**(4622), 1524 (1958). Publisher: Nature Publishing Group, URL <https://www.nature.com/articles/1811524a0>.
- [39] X. He, G. I. Harris, C. G. Baker, A. Sawadsky, Y. L. Sfendla, Y. P. Sachkou, S. Forstner, and W. P. Bowen. *Strong optical coupling through superfluid Brillouin lasing.* Nature Physics **16**(4), 417 (2020). Publisher: Nature Publishing Group, URL <https://www.nature.com/articles/s41567-020-0785-0>.

- [40] A. D. Kashkanova, A. B. Shkarin, C. D. Brown, N. E. Flowers-Jacobs, L. Childress, S. W. Hoch, L. Hohmann, K. Ott, J. Reichel, and J. G. E. Harris. *Superfluid Brillouin optomechanics*. Nature Physics **13**(1), 74 (2017). Publisher: Nature Publishing Group, URL <https://www.nature.com/articles/nphys3900>.
- [41] D. McAuslan, G. Harris, C. Baker, Y. Sachkou, X. He, E. Sheridan, and W. Bowen. *Microphtonic Forces from Superfluid Flow*. Physical Review X **6**(2), 021012 (2016). Publisher: American Physical Society, URL <https://link.aps.org/doi/10.1103/PhysRevX.6.021012>.
- [42] G. I. Harris, D. L. McAuslan, E. Sheridan, Y. Sachkou, C. Baker, and W. P. Bowen. *Laser cooling and control of excitations in superfluid helium*. Nature Physics **12**(8), 788 (2016). Publisher: Nature Publishing Group, URL <https://www.nature.com/articles/nphys3714>.
- [43] F. M. Ellis and R. B. Hallock. *High-resolution third-sound resonator*. Review of Scientific Instruments **54**(6), 751 (1983). URL <https://doi.org/10.1063/1.1137468>.
- [44] J. A. Hoffmann, K. Penanen, J. C. Davis, and R. E. Packard. *Measurements of Attenuation of Third Sound: Evidence of Trapped Vorticity in Thick Films of Superfluid ${}^4\text{He}$* . Journal of Low Temperature Physics **135**(3), 177 (2004). URL <https://doi.org/10.1023/B:JOLT.0000024548.03525.cd>.
- [45] K. A. Wilson and F. Vollmer. *Whispering Gallery Mode Resonator Biosensors*. In B. Bhushan, ed., *Encyclopedia of Nanotechnology*, pp. 4387–4401 (Springer Netherlands, Dordrecht, 2016). URL https://doi.org/10.1007/978-94-017-9780-1_121.
- [46] R. J. Donnelly and C. F. Barenghi. *The Observed Properties of Liquid Helium at the Saturated Vapor Pressure*. Journal of Physical and Chemical Reference Data **27**(6), 1217 (1998). URL <https://doi.org/10.1063/1.556028>.
- [47] P. L. Marston and W. M. Fairbank. *The Free Surface of Rotating ${}^4\text{He}$ Thick Films*. In S. B. Trickey, E. D. Adams, and J. W. Dufty, eds., *Quantum Fluids and Solids*, pp. 411–420 (Springer US, Boston, MA, 1977). URL http://link.springer.com/10.1007/978-1-4684-2418-8_48.
- [48] E. B. Sonin and A. J. Manninen. *Downfall of the vortex dimple in superfluids*. Physical Review Letters **70**(17), 2585 (1993). Publisher: American Physical Society, URL <https://link.aps.org/doi/10.1103/PhysRevLett.70.2585>.
- [49] J. R. Seddon, M. S. Thurlow, and P. G. Lucas. *Quantised vortex visualisation*. Journal of Low Temperature Physics **138**(3), 499 (2005). URL <https://doi.org/10.1007/s10909-005-2241-z>.
- [50] L. Chrostowski and M. Hochberg. *Silicon Photonics Design: From Devices to Systems* (Cambridge University Press, Cambridge, 2015). URL <https://www.cambridge.org/core/books/silicon-photonics-design/BF3CF13E8542BCE67FD2BBC7104ECEAB>.

- [51] L. P. Pitaevskii and S. Stringari. *Bose-Einstein condensation and superfluidity*. No. 164 in International series of monographs on physics (Oxford University Press, Oxford, United Kingdom, 2016), first edition ed. OCLC: ocn919186901.
- [52] Z. Mehdi, J. J. Hope, S. S. Szigeti, and A. S. Bradley. *Mutual friction and diffusion of two-dimensional quantum vortices*. Physical Review Research **5**(1), 013184 (2023). URL <https://link.aps.org/doi/10.1103/PhysRevResearch.5.013184>.
- [53] M. Reeves, T. Billam, B. Anderson, and A. Bradley. *Identifying a Superfluid Reynolds Number via Dynamical Similarity*. Physical Review Letters **114**(15), 155302 (2015). URL <https://link.aps.org/doi/10.1103/PhysRevLett.114.155302>.
- [54] C. Pethick and H. Smith. *Bose-Einstein condensation in dilute gases* (Cambridge University Press, Cambridge ; New York, 2002).
- [55] M. Tsubota, K. Kasamatsu, and M. Ueda. *Vortex lattice formation in a rotating Bose-Einstein condensate*. Physical Review A **65**(2), 023603 (2002). Publisher: American Physical Society, URL <https://link.aps.org/doi/10.1103/PhysRevA.65.023603>.
- [56] P. Blakie†, A. Bradley†, M. Davis, R. Ballagh, and C. Gardiner. *Dynamics and statistical mechanics of ultra-cold Bose gases using c-field techniques*. Advances in Physics **57**(5), 363 (2008). Publisher: Taylor & Francis _eprint: <https://doi.org/10.1080/00018730802564254>, URL <https://doi.org/10.1080/00018730802564254>.
- [57] M. T. M. Christenhusz, A. Safavi-Naini, H. Rubinsztein-Dunlop, T. W. Neely, and M. T. Reeves. *Emergent Universal Drag Law in a Model of Superflow* (2024). ArXiv:2406.14049, URL <http://arxiv.org/abs/2406.14049>.
- [58] M. Reeves. *Quantum Analogues of Two-Dimensional Classical Turbulence*. Ph.D. thesis, University of Otago (2017).
- [59] G. R. Dennis, J. J. Hope, and M. T. Johnsson. *XMDs2: Fast, scalable simulation of coupled stochastic partial differential equations*. Computer Physics Communications **184**(1), 201 (2013). URL <https://www.sciencedirect.com/science/article/pii/S0010465512002822>.
- [60] O. R. Stockdale, M. T. Reeves, and M. J. Davis. *Dynamical Mechanisms of Vortex Pinning in Superfluid Thin Films*. Physical Review Letters **127**(25), 255302 (2021). URL <https://link.aps.org/doi/10.1103/PhysRevLett.127.255302>.
- [61] R. Marchetti, C. Lacava, L. Carroll, K. Gradkowski, and P. Minzioni. *Coupling strategies for silicon photonics integrated chips*. Photonics Research **7**(2), 201 (2019). Publisher: Optica Publishing Group, URL <https://opg.optica.org/prj/abstract.cfm?uri=prj-7-2-201>.
- [62] W. Bogaerts and L. Chrostowski. *Silicon Photonics Circuit Design: Methods, Tools and Challenges*. Laser & Photonics Reviews **12**(4), 1700237 (2018). URL <https://onlinelibrary.wiley.com/doi/abs/10.1002/lpor.201700237>.

- [63] S. M. Meenehan, J. D. Cohen, S. Gröblacher, J. T. Hill, A. H. Safavi-Naeini, M. Aspelmeyer, and O. Painter. *Silicon optomechanical crystal resonator at millikelvin temperatures*. Physical Review A **90**(1), 011803 (2014). Publisher: American Physical Society, URL <https://link.aps.org/doi/10.1103/PhysRevA.90.011803>.
- [64] S. Khan, S. M. Buckley, J. Chiles, R. P. Mirin, S. W. Nam, and J. M. Shainline. *Low-loss, high-bandwidth fiber-to-chip coupling using capped adiabatic tapered fibers*. APL Photonics **5**(5), 056101 (2020). URL <https://doi.org/10.1063/1.5145105>.
- [65] R. Rivière, O. Arcizet, A. Schliesser, and T. J. Kippenberg. *Evanescence straight tapered-fiber coupling of ultra-high Q optomechanical micro-resonators in a low-vibration helium-4 exchange-gas cryostat*. Review of Scientific Instruments **84**(4), 043108 (2013). URL <https://doi.org/10.1063/1.4801456>.
- [66] S. Gröblacher, J. T. Hill, A. H. Safavi-Naeini, J. Chan, and O. Painter. *Highly efficient coupling from an optical fiber to a nanoscale silicon optomechanical cavity*. Applied Physics Letters **103**(18), 181104 (2013). URL <https://doi.org/10.1063/1.4826924>.
- [67] R. Osgood and X. Meng. *Principles of Photonic Integrated Circuits: Materials, Device Physics, Guided Wave Design*. Graduate Texts in Physics (Springer International Publishing, Cham, 2021). URL <https://link.springer.com/10.1007/978-3-030-65193-0>.
- [68] T. G. Tiecke, K. P. Nayak, J. D. Thompson, T. Peyronel, N. P. d. Leon, V. Vuletić, and M. D. Lukin. *Efficient fiber-optical interface for nanophotonic devices*. Optica, Vol. 2, Issue 2, pp. 70-75 (2015). Publisher: Optica Publishing Group, URL <https://opg.optica.org/optica/abstract.cfm?uri=optica-2-2-70>.
- [69] M. Küppers, D. Albrecht, A. D. Kashkanova, J. Lühr, and V. Sandoghdar. *Confocal interferometric scattering microscopy reveals 3D nanoscopic structure and dynamics in live cells*. Nature Communications **14**(1), 1962 (2023). Publisher: Nature Publishing Group, URL <https://www.nature.com/articles/s41467-023-37497-7>.
- [70] M. Dahmardeh, H. Mirzaalian Dastjerdi, H. Mazal, H. Köstler, and V. Sandoghdar. *Self-supervised machine learning pushes the sensitivity limit in label-free detection of single proteins below 10 kDa*. Nature Methods **20**(3), 442 (2023). Publisher: Nature Publishing Group, URL <https://www.nature.com/articles/s41592-023-01778-2>.
- [71] E. S. Sabisky and C. H. Anderson. *Onset for Superfluid Flow in He 4 Films on a Variety of Substrates*. Physical Review Letters **30**(22), 1122 (1973). URL <https://link.aps.org/doi/10.1103/PhysRevLett.30.1122>.
- [72] A. R. Korsch, N. Fiaschi, and S. Gröblacher. *Phononic crystals in superfluid thin-film helium*. Physical Review Applied **22**(4), L041005 (2024). URL <https://link.aps.org/doi/10.1103/PhysRevApplied.22.L041005>.

- [73] Y. Sachkou. *Theoretical Investigation of Vortex-Sound Interactions in Two-Dimensional Superfluids*. In Y. Sachkou, ed., *Probing Two-Dimensional Quantum Fluids with Cavity Optomechanics*, pp. 75–99 (Springer International Publishing, Cham, 2020). URL https://doi.org/10.1007/978-3-030-52766-2_4.
- [74] C. Bekker, R. Kalra, C. Baker, and W. P. Bowen. *Injection locking of an electro-optomechanical device*. Optica **4**(10), 1196 (2017). Publisher: Optica Publishing Group, URL <https://opg.optica.org/optica/abstract.cfm?uri=optica-4-10-1196>.
- [75] K. C. Harvey and A. L. Fetter. *Free surface of a rotating superfluid*. Journal of Low Temperature Physics **11**(3), 473 (1973). URL <https://doi.org/10.1007/BF00656564>.